Archive of Applied Mechanics (2023) 93:891–912
https://doi.org/10.1007/s00419-022-02327-7

REVIEW

Wen-Shinn Shyu · Wen-Cheng Yeh

Determining anti-plane responses of symmetric canyon embedded within single-layer half-space

Received: 20 May 2022 / Accepted: 11 November 2022 / Published online: 17 December 2022

Abstract This paper proposes a modified hybrid method combining finite element method and a Lamb series, to derive the displacement amplitude of a symmetric canyon embedded within a single-layer half-space subjected to shear horizontal (*SH*) waves. Four canyon shapes and various site effects were also examined under various incident angles and dimensionless frequencies. The site effects included the canyon-decay effects and canyon-area effects (due to the existing canyon) as well as the thickness effect (due to the soft layer). We discuss the resonance frequencies of the single-layer half-space under various shifts in incident angle imposed by the existed canyon. We also compare the responses obtained in this paper with those of a canyon embedded in a half-space. Finally, we employed the fast Fourier transform to obtain responses in the time domain with series responses in the frequency domain. These results support our discovery that site effects dominated responses at the free surface. This paper provides a valuable reference furthering our understanding of site effects associated with surface irregularities in a single-layer half-space.

Keywords *SH* waves · Single-layer half-space · Symmetric canyon · Hybrid method · Ricker wavelet

1 Introduction

Irregular surface topographies, including canyons and alluvial valleys or hills, generate site effects capable of affecting seismic waves. Pronounced surface responses (such as displacement, velocity, or acceleration) appear in various site locations, for example, the rim of canyons [1, 2], the central area of alluvial valleys [2, 3], and the top of hills [2, 4–6]. These results can be observed in seismic records [1, 7]. Numerous simulations of the site effects have been conducted over the last four decades. However, valuable seismic records are not easily obtained, due to a lack of seismographs and/or strong ground motion. Thus, the analysis of the site effects relies heavily on numerical simulations, including the wave function expansion method [1, 3, 5, 6, 8–11], boundary element method [4, 12–15], pseudo-spectral method [16], and hybrid method [2, 17–24]. In most research papers, problems related to scattering have been simplified through the use of an isotropic homogeneous model, despite the fact that the most of the materials in the earth's crust are anisotropic, due to effects of sediment deposition and weathering [25]. Under these conditions, a layered medium tends to be far closer to the ground truth than is a homogeneous isotropic half-space. Thomson [26], Kennett and Kerry [27] introduced the propagator matrix method to study responses within a multilayer half-space. Nguyen and Tassoulas used a reciprocal absorbing boundary condition combined with perfectly matched discrete layers to discuss the propagation of *SH* waves in a layered half-space [28]. Their approach allows surface irregularities embedded in the layered half-space to produce wave propagation responses of greater complexity via scattering

W.-S. Shyu · W.-C. Yeh (✉)
Department of Civil Engineering, National Pingtung University of Science and Technology, 1, Shuefu Road, Neipu 91201, Pingtung, Taiwan, ROC
e-mail: weyeh@mail.npust.edu.tw

and diffraction. In the last decade, many researchers have focused on the problems of scattering related to irregularities embedded within (or crossing through) a layered half-space. A number of recent studies have employed indirect boundary element methods to investigate the surface responses of a layered half-space with various irregularities, including an alluvial valley [29], a hill [30], an earth dam [31], a canyon [32–34], and topographic features [35, 36]. Numerical methods such as wave function expansion have also been used to model the layer-effect of a circular-arc canyon embedded within a double-stratified half-space [37]. In a previous study, the wave function expansion was used to solve a *P* wave scattering problem pertaining to a layer-interface crossing a V-shaped canyon [38]. To discuss the phenomena due to the complex topography, the ratio of characteristic length of topography to the incident wavelength was convenient to analyze the amplification and interference effects due to incident waves scattering problem [1, 2].

Over last six years, the hybrid method used in the references above [18–21, 23, 24] has been applied to the problem of an isotropic half-space with irregularities. In addition, the problem of scattering associated with an alluvial valley embedded within a single-layer half-space has been resolved [22]. We previously developed a series function to represent the scattering of waves in a single-layer half-space in the formulation of a matrix equation for the modified hybrid method. In this current study, we extended our experiments to symmetric canyons embedded within a single-layer half-space. The formulation of an alluvial valley can be attributed to the accumulation of sedimentary soil within a canyon. It is for this reason that canyons embedded within a single-layer half-space are a common topographical feature. For example, a U-shaped canyon forms when a glacier travels across and down a slope, whereas a V-shaped canyon in cross section is carved out when a river traverses a similar slope [25]. We therefore developed symmetric canyons of various shapes, including a semicircle, a shallow semi-ellipse, a trapezium, and a triangle in cross section. We meshed the various canyons using the transfinite interpolation (TFI) function [39] to obtain the nodal coordinates required for FEM calculations. We then introduced incident *SH* waves with specified resonance frequencies (*RF*s) in a single-layer half-space (in accordance with previous study) [22] to facilitate the analysis of site effects. In the current study, we verified the accuracy of sequenced frequency results to ensure the accuracy of our results under relatively high frequencies. This was achieved by combining the Ricker wavelet [8, 10] with canyon surface responses in the frequency domain in order to obtain displacements in the time domain. Takemiya and Fujiwara also employed BEM in the time domain to facilitate computation involving *SH* wave propagation at irregular sites embedded within the half-space [14]. Site effects proved helpful to our analysis in both the frequency and time domains.

2 Methodology

2.1 Model

Figure 1 presents a two-dimensional (2-D) model that includes a soft layer (Ω^1) of thickness H on a hard bedrock half-space (Ω^2) with interface L on the x–z plane. A symmetric canyon with width $2a$and depth d is enclosed as Ω^0 with boundary C entirely embedded within the soft layer, such that the depth of the canyon is less than the thickness of the soft layer (i.e., $d < H$). An anti-plane incident *SH* wave with circular frequency ω and incident angle θ_2 impinges on this topography. In the anti-plane model, only responses along the y-direction can occur. Each of the materials in the soft layer and hard bedrock is isotropic and elastic, wherein densities (ρ_j) and shear modulus (μ_j) can be used to obtain the shear velocity ($C_{sj} = \sqrt{\mu_j / \rho_j}$). Note that $j = 1,\ 2$, respectively, refer to different materials of Ω^1 and Ω^2. Note also that the materials of Ω^0 are equivalent to those of Ω^1.

Our numerical modeling scheme was used to examine the problem of scattering by a symmetric canyon embedded within the single-layer half-space which is presented as follows:

(1) A short introduction to displacement responses and stress associated with incident *SH* waves within a followed the reference single-layer half-space is presented in Sect. 2.2.
(2) The surface displacement responses in the single-layer half-space to identify important incident angles and relative resonance frequencies are examined in Sect. 2.3.
(3) The hybrid method combining the series scattering function of a single-layer half-space is introduced in Sect. 2.4.
(4) The use of a novel hybrid method to deal with the problem of scattering by a symmetric canyon embedded within a single-layer half-space is also introduced in Sect. 3.

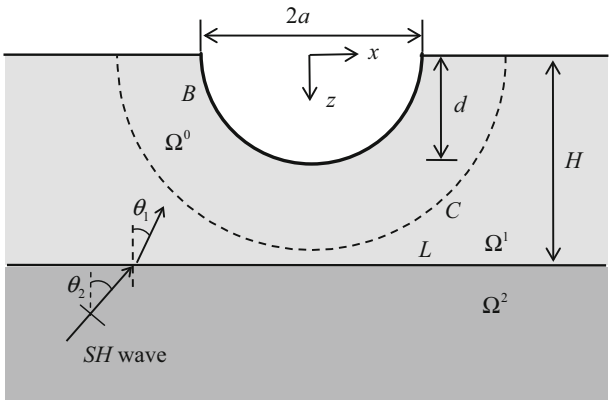

Fig. 1 Schematic diagram showing symmetric canyon with width $2a$ and depth d embedded within a soft layer of depth H above the half-space

(5) Finally, the Ricker wavelet used to derive surface responses in the time domain is introduced in Sect. 4.

2.2 Equations of SH waves propagation in single-layer half-space

As outlined in reference [22], the incident displacement (u^i_{yj}) and reflective displacement (u^r_{yj}) due to an incident *SH* wave impinging on a single-layer half-space without an existing canyon can be derived as follows:

In the soft soil layer (i.e., $z \le H$),

$$u^i_{y1} = A_1 e^{-\mathrm{i}(\xi_1 x - \beta_1 z)} \quad \text{and} \quad u^r_{y1} = B_1 e^{-\mathrm{i}(\xi_1 x + \beta_1 z)} \tag{1}$$

And in the half-space bedrock (i.e., $z > H$),

$$u^i_{y2} = A_2 e^{-\mathrm{i}(\xi_2 x - \beta_2 z)} \quad \text{and} \quad u^r_{y2} = B_2 e^{-\mathrm{i}(\xi_2 x + \beta_2 z)} \tag{2}$$

where $\mathrm{i} = \sqrt{-1}$, $\xi_j = k_{sj} \sin\theta_j$ and $\beta_j = k_{sj} \cos\theta_j$ represent the apparent wave numbers, and k_{sj} represents the wave number derived using the following formula: $\omega = k_{sj} C_{sj}$. As shown in Fig. 1, θ_1 is the refractive angle obtained using Snell's law equal to $\sin^{-1}\left(C_{s1} \sin\theta_2 / C_{s2}\right)$. It can be regarded as a new incident angle in Ω^1. The unit amplitude of incident waves can be derived as $A_2 = 1.0$, and the relative coefficients can be derived as follows:

$$A_1 = B_1 = \frac{\cos Q_2 + \mathrm{i} \sin Q_2}{\cos Q_1 + \mathrm{i} P \sin Q_1} A_2 \tag{3a}$$

$$B_2 = (\cos Q_2 + \mathrm{i} \sin Q_2)(\cos Q_1 - \mathrm{i} P \sin Q_1) A_1 \tag{3b}$$

where

$$P = \frac{\mu_1 \beta_1}{\mu_2 \beta_2}, \tag{3c}$$

$$Q_j = \beta_j H; j = 1,\ 2. \tag{3d}$$

Thus, we can obtain the displacements (u^f_{yj}), stresses (σ^f_{xyj}, and σ^f_{zyj}), and tractions (t^f_{yj}) in the free field (represented by superscript f), including the contributions from incident and reflected plane waves as follows:

$$u^f_{yj} = u^i_{yj} + u^r_{yj}; j = 1,\ 2 \tag{4a}$$

$$\sigma^f_{xyj} = \sigma^i_{xyj} + \sigma^r_{xyj}, \sigma^f_{zyj} = \sigma^i_{zyj} + \sigma^r_{zyj}; j = 1,\ 2 \tag{4b}$$

$$t^f_{yj} = \sigma^f_{xyj} n_x + \sigma^f_{zyj} n_z; j = 1,\ 2 \tag{4c}$$

where n_x and n_z are the components of the unit normal vector, respectively, in the x and z directions.

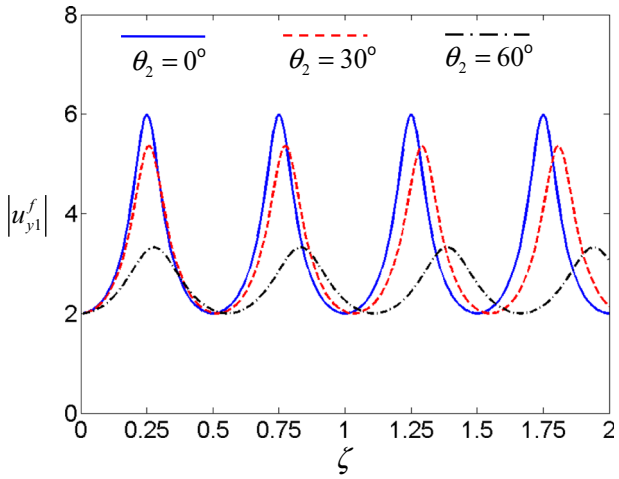

Fig. 2 Free surface displacement of single-layer half-space impinged by incident waves with a various incident angle θ_2

2.3 Surface displacement amplitudes of single-layer half-space

In accordance with the formulae in Sect. 2.2, it is possible to derive the theoretical amplitudes of displacement in a single-layer half-space (i.e., $\left|u^f_{yj}\right|$) impinged by incident *SH* waves, including the soft layer Ω^1 (i.e., $\left|u^f_{y1}\right|$) and the hard bedrock Ω^2 (i.e., $\left|u^f_{y2}\right|$), based on the following assumptions. The material properties are set at $\mu_1 = 1.0$ and $\rho_1 = 1.0$ in Ω^1 with $\mu_2 = 6\mu_1$ and $\rho_2 = 1.5\rho_1$ in Ω^2, leading to shear wave speeds $C_{s1} = 1.0$ and $C_{s2} = 2.0$. According to the Snell's law and the relative coefficients of incident waves (and reflective waves) discussed in 2.2, it could be obtained with the given ratio of materials (i.e., shear modulus and density, or wave speed). Hence, we could choose the wave speeds $C_{s1} = 1.0$ and $C_{s2} = 2.0$, which equals $C_{s2}/C_{s1} = 2.0$. It was helpful to simplify the problem. The values of refractive angle (θ_1) due to various incident angles and the changes in wave speed crossing boundary L can be obtained using Snell's law as follows: 0° (due to $\theta_2 = 0°$), 14.48° (due to $\theta_2 = 30°$), and 25.66° (due to $\theta_2 = 60°$). Generally, the value of θ_1 is only one half that of θ_2, with the result that the incident waves in Ω^1 are nearly vertical ($0° \le \theta_2 \le 60°$).

Following the convenient parameter introduced from Trifunac [1, 2], we use the ratio of the thickness of the soft layer (H) to the wavelength of the incident shear waves (λ_1) in Ω^1. Then, we define a dimensionless frequency $\zeta = H/\lambda_1$. We also use the relationship between wavelength and wave number (k_s) (i.e., $\lambda_1 = 2\pi/k_{s1}$) to derive $\zeta = \omega H/2\pi C_{s1}$. Based on the above material properties, the theoretical results of $\left|u^f_{y1}(x,0)\right|$ versus ζ on the free surface of a single-layer half-space are presented in Fig. 2. Note that the values of $\left|u^f_{y1}(x,0)\right|$ in horizontal position x are independent, such that $\left|u^f_{y1}(x,0)\right|$ can be shortened as $\left|u^f_{y1}\right|$. The solid blue line, dashed red line, and dash-dot black line, respectively, represent variations in displacement associated with ζ under $\theta_2 = 0°$, 30°, and 60°. For a given ζ value ranging from 0.01 to 2.0, it was possible to obtain a response value for $\left|u^f_{y1}\right|$ at the free surface. Note, however, that some ζ values occurring at the resonance frequency (*RF*) generated large $\left|u^f_{y1}\right|$ values. The highest $\left|u^f_{y1}\right|$ values and corresponding ζ values were nearly the same under $\theta_2 = 0°$ and 30°; therefore, Table 1 and Table 2 list only the ζ values obtained under $\theta_2 = 0°$ and 60°. We identified ζ^M_n ($n = 1,\ 2,\ 3,\ 4$) as the first to fourth modes of the *RF*s generating the highest $\left|u^f_{y1}\right|$ values (i.e., $\left|u^{fM}_{y1}\right|$) at the surface (see Table 1). We then identified ζ^m_n ($n = 1,\ 2,\ 3,\ 4$) as the first to fourth modes of the *RF*s generating the lowest $\left|u^f_{y1}\right|$ values (i.e., $\left|u^{fm}_{y1}\right|$) at the surface (see Table 2). We observed only three *RF*s of ζ^m_n under $\theta_2 = 60°$ over the range of values discussed above. Further details can be found in the discussion section of a paper previously published by the authors [22].

Table 1 Maximum absolute values of free surface displacement and corresponding frequencies under $\theta_2 = 0°$ and 60°

	$\left\|u_{y1}^{fM}\right\|$	ζ_1^M	ζ_2^M	ζ_3^M	ζ_4^M
$\theta_2 = 0°$	6.00	0.25	0.75	1.25	1.75
$\theta_2 = 60°$	3.33	0.28	0.83	1.39	1.94

Table 2 Minimum absolute values of free surface displacement and corresponding frequencies under $\theta_2 = 0°$ and 60°

	$\left\|u_{y1}^{fm}\right\|$	ζ_1^m	ζ_2^m	ζ_3^m	ζ_4^m
$\theta_2 = 0°$	2.00	0.50	1.00	1.50	2.00
$\theta_2 = 60°$	2.00	0.56	1.11	1.66	–

2.4 Hybrid method with series functions introduced in single-layer half-space

The hybrid method combining FEM with series functions was developed to deal with the anti-plane problem of scattering due to surface irregularities in a half-space [2, 16–22]. In formulating the mass matrix and stiffness matrix for FEM, we meshed irregular region Ω^0 with a semicircular boundary C using the TFI formula, based on the details outlined in our previous work [16]. The series functions were based on the anti-plane Lamb load in the half-space (or in the single-layer half-space). Thus, the hybrid method is essentially a combination of FEM with a Lamb series formulated as a matrix equation as follows:

$$\begin{bmatrix} \mathbf{K}^{aa} - \omega^2\mathbf{M}^{aa} & -\mathbf{K}^{ac} \\ -\mathbf{K}^{ca} & \mathbf{K}^{cc} \end{bmatrix} \begin{Bmatrix} \mathbf{u}_{y0} \\ \mathbf{c} \end{Bmatrix} = \begin{Bmatrix} \mathbf{P}^a \\ -\mathbf{P}^c \end{Bmatrix} \tag{5}$$

where $\left[\mathbf{K}^{aa}\right]$ and $\left[\mathbf{M}^{aa}\right]$, respectively, represent the stiffness matrix and mass matrix obtained using the FEM formulation, $\{\mathbf{P}^a\}$ refers to the force vector from the product of the traction of the free field and the displacement at boundary C, and $\{\mathbf{P}^c\}$ refers to the force vector from the product of the displacement of the free field and the traction of the scattered field at boundary C. $\left[\mathbf{K}^{ac}\right]$ and $\left[\mathbf{K}^{ca}\right]$ indicate the coupling matrices formed by combining displacement in Ω^0 with the traction of the scattered field at boundary C. $\left[\mathbf{K}^{cc}\right]$ indicates the matrix formed by combining the traction and displacement of the scattered field at boundary C. Vector $\left\{\mathbf{u}_{y0}\right\}$ refers to the displacements of each node in region Ω^0, whereas vector $\{\mathbf{c}\}$ refers to the unknown coefficients in the scattered field. In one previous study [19], we altered the series function using in-plane scattering waves to resolve the problem of wave scattering due to P waves. In another previous study, the scattering of waves in a single-layer half-space was used to resolve the problem of scattering due to an alluvial valley embedded within the single-layer half-space [22]. This approach was meant to extend the range problems that can be solved using the hybrid method. In the current study, we used the hybrid method to examine the site effects of a canyon embedded within a single-layer half-space. The formula of series functions was shown to satisfy the boundary conditions of a single-layer half-space, as shown in "Appendix 1".

3 Results and discussion

3.1 The responses of displacement at free surface

In this paper, the symmetric canyon was embedded in the soft layer of a half-space. As shown in Table 3, we examined four types of canyon: the semicircular (Case 1), triangular (Case 2), trapezoidal (Case 3), and shallow semi-elliptical (Case 4). The ratio of the deepest canyon depth (d) to the half-width of the canyon (a) was set to 1.00, except in Case 4 (0.75). The thickness of the soft layer was set at $H = 2a$, which means that the symmetric canyon was embedded entirely within the soft layer. Thus, the irregular region Ω^0 including the canyon (referred to as the physical region) was bounded by a portion of the free surface and a semicircle with radius $1.5a$(auxiliary boundary C), as shown in Fig. 1. To mesh region Ω^0, we used the transform equation of transfinite interpolation (TFI) to calculate nodal coordinates within Ω^0 in order to obtain the sequence of nodal points. Details pertaining to use TFI can be found in a previous study by the author [16]. Figure 3 presents the FEM meshed grids of Ω^0 in Case 1 (semicircular canyon), Case 2 (triangular canyon), Case 3 (trapezoid

Table 3 Dimensionless parameters of symmetric canyons of four types

	Canyon shape	d/a	(area of canyon)$/a^2$
Case 1	Semicircular canyon	1.00	1.57
Case 2	Triangular canyon	1.00	1.00
Case 3	Trapezoid canyon	1.00	1.50
Case 4	Shallow semi-elliptical canyon	0.75	1.18

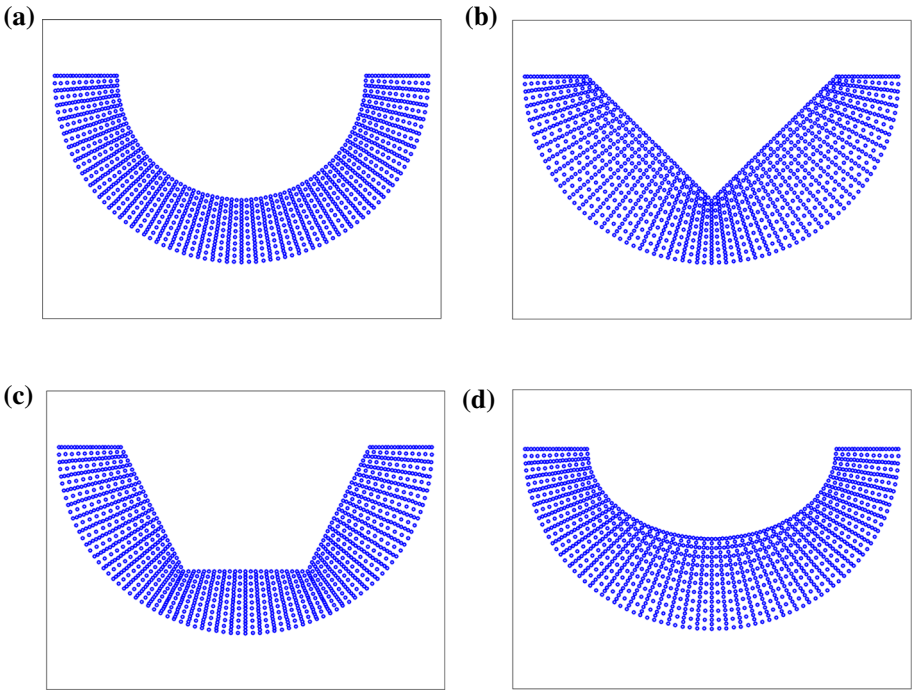

Fig. 3 FEM mesh of Ω^0 including (**a**) semicircular canyon (Case 1), (**b**) triangular canyon (Case 2), (**c**) trapezoidal canyon (Case 3), and (**d**) shallow semi-elliptical canyon (Case 4)

canyon), and Case 4 (shallow semi-elliptical canyon), in which each case included 400 Q8 elements and 1301 nodes.

3.2 Verification of single-layer half-space model via degeneration

Though the authors did their best, the similar problems were fewer in the previous study. However, depending on the successful experiment in solving the anti-plane scattering problem in a single-layer half-space [22], it prompted us to extend a similar procedure to solve for different topographies. Nonetheless, we were unable to find a similar model in previous studies. We therefore sought to verify our numerical results by degenerating the single-layer half-space model into a half-space model. We used the parameters in Ω^2 and Ω^0 in Ω^1, as follows: $\mu = 1.0$ and $\rho = 1.0$ (i.e., $C_s = 1.0$). These led to dimensionless frequency $\zeta = \omega a/2\pi C_s$. The curves in Fig. 4 produced variations in $|u_y|$, where x/a at $\theta_2 = 0°$ (Fig. 4a) and $\theta_2 = 60°$ (Fig. 4b) under $\zeta = 0.25$ (i.e., ζ_1^M), as well as at $\theta_2 = 0°$ (Fig. 4c) and $\theta_2 = 60°$ (Fig. 4d) under $\zeta = 0.75$ (i.e., ζ_2^M). The numerical results obtained are shown using four curves: solid blue line (Case I), dashed red line (Case II), dash-dot black line (Case III), and dash-dot pink line (Case IV). Cases I to IV use the shape of the symmetric canyon in Cases 1 to 4 embedded within the half-space. These symbols, respectively, represent the numerical results obtained by the author in a previous work [2]. As shown in Fig. 4a–d, the numerical results obtained in the current study are in reasonable agreement with those obtained in the previous work. Note that the dashed light-blue line represents the response of $|u_y^f|$. Note also that the uniform value (i.e., 2.0) is an arbitrary value independent of position (x/a), incident angle (θ_2), and dimensionless frequency (ζ).

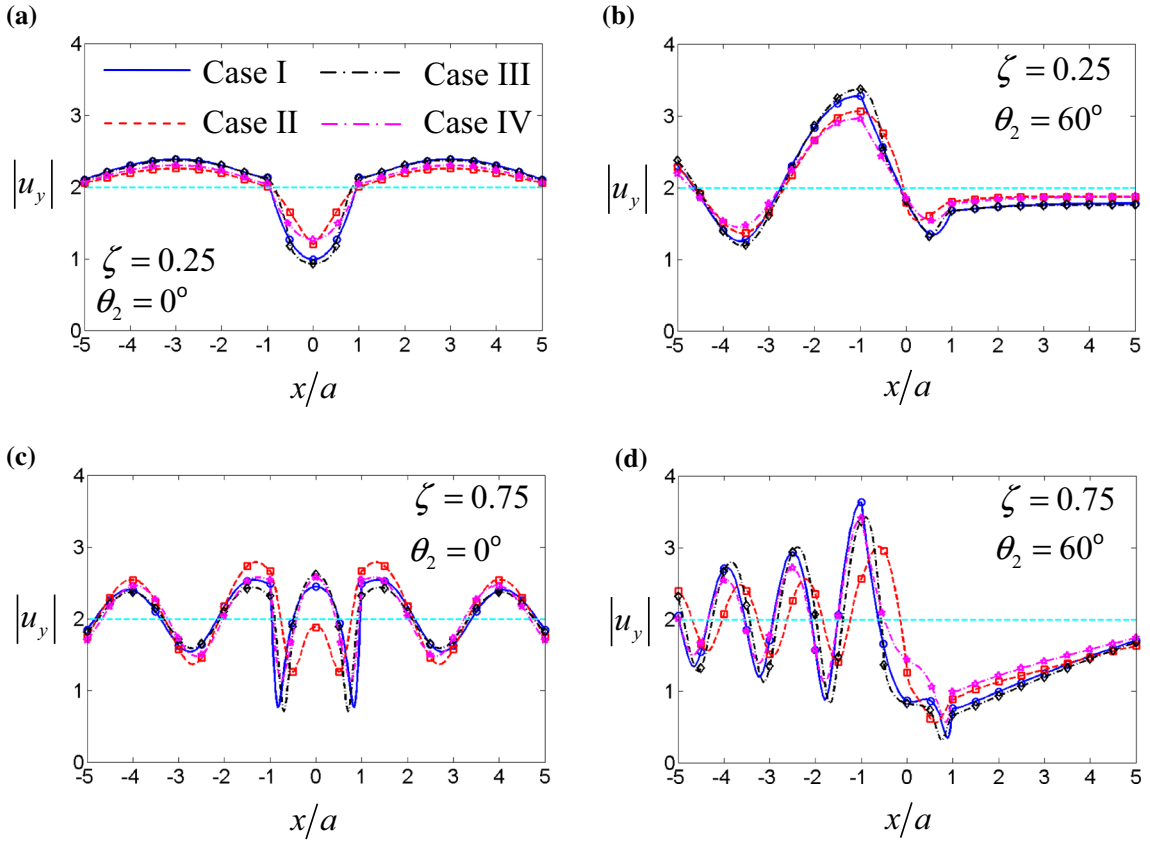

Fig. 4 Variations in surface response $|u_y|$ of canyon embedded in half-space including (**a**) $\theta_2 = 0°$ and (**b**) $\theta_2 = 60°$ with $\zeta = 0.25$ and (**c**) $\theta_2 = 0°$ and (**d**) $\theta_2 = 60°$ with $\zeta = 0.75$, where the circles, squares, and diamonds indicate results reported by Shyu et al. [2]

In Fig. 4, we investigated asymptotic variations in $|u_y|$ resulting from a series of changes in the shape of the canyon by calculating the responses in Case I to Case IV. In Fig. 4a and c, the symmetric responses of $|u_y|$ are due to the symmetric shapes of a canyon, where $\theta_2 = 0°$. The maximum value of $|u_y|$ (i.e., $|u_y^M|$) tended to occur at the corner of the canyon; however, the minimum value of $|u_y|$ (i.e., $|u_y^m|$) occurred at the bottom of a canyon with a relatively low dimensionless frequency (e.g., $\zeta = 0.25$). Note that $|u_y^M|$ occurred in the canyon corner as well as the bottom of the canyon; however, $|u_y^m|$ occurred adjacent to the side of the canyon with a relatively high dimensionless frequency (e.g., $\zeta = 0.75$). A smaller wavelength ($\lambda = (2a) \times 4/3$ for $\zeta = 0.75$) would almost allow insertion of the canyon, leading to a pair of wave crests and wave troughs. In Fig. 4b and d, the evolution following an oscillation in $|u_y|$ in the illuminated zone (i.e., $x/a < -1.0$) to the decay of $|u_y|$ in the shadow zone (i.e., $x/a > 1.0$) was sufficient to suppress the canyon-decay effect [15] of $|u_y|$ along the free surface of the canyon (i.e., $-1.0 \le x/a \le 1.0$). Following an increase in ζ, the corresponding increase in oscillation in the illuminated zone led to an increase in $|u_y^M|$ in the left corner of the canyon. A sharp canyon-decay effect along the canyon surface led to $|u_y^m|$ adjacent to the right corner. Due to the shielding effect [16], the responses to $|u_y|$ in the shadow zone rapidly approached $|u_y^f|$ with an increase in ζ. We observed that the values of $|u_y^M|$ (and $|u_y^m|$) were affected by the shape of canyon, particularly the slope discontinuous point(s) (SDCPs) within a non-smooth canyon (NSC) [18], such as in Cases II and III. The

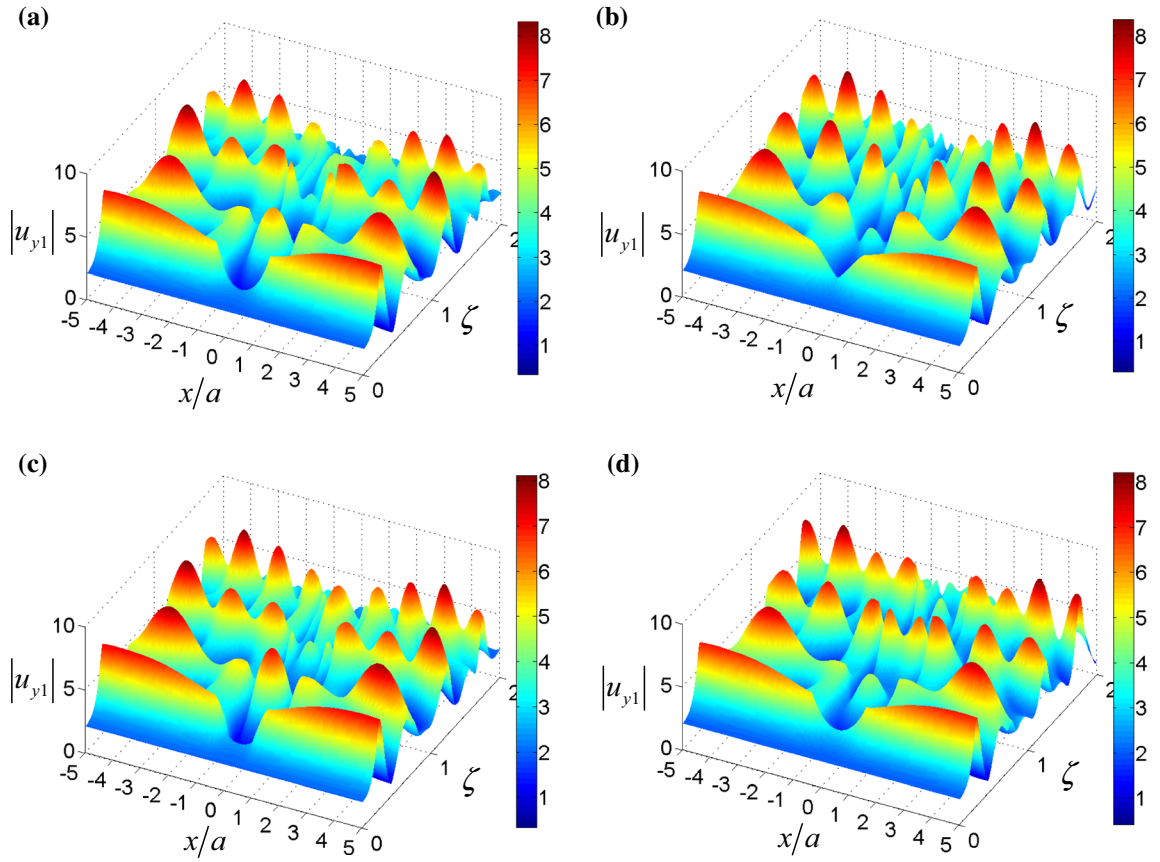

Fig. 5 Variations in $|u_{y1}|$ on free surface of single-layer half-plane where $\theta_2 = 0°$ with $-5 \le x/a \le 5$ in four types of canyon: (**a**) Case 1; (**b**) Case 2; (**c**) Case 3; and (**d**) Case 4

combined effects of SDCP and canyon corner points caused fluctuations in displacements, which produced the smallest $|u_y^M|$ (and $|u_y^m|$) values in Case II.

3.3 The transfer functions of specific locations at canyon surface embedded in single-layer half-space

We display the free surface responses ($|u_y|$) of a symmetric canyon embedded in a single-layer half-space under various ζ by 3-D plots of surface displacement amplitudes in Cases 1 to 4 with *SH* waves at various incident angles ($\theta_2 = 0°$ and 60°) (see Figs. 5 and 6). Using the materials introduced in Sect. 2.3, ζ was ranging from 0.01 to 2.0, and the dimensionless distance (x/a) was ranging from -5 to 5. In Fig. 5, the effects of canyon shape were obvious under low ζ values where $\theta_2 = 0°$. When ζ was increased, the value of $|u_y|$ in the surface of the triangular canyon was smaller than at the surface of the other canyons, as shown in Fig. 5b. The responses at the surface of shallow canyons were more pronounced than those at the surface of deeper canyons, due to a weakening of the canyon-decay effect, such as Case 4 in Fig. 5d. Canyons with smaller areas (i.e., Cases 1 and 3 in Table 3) generated similar response patterns, except in regions close to the SDCPs. As shown in Fig. 6, the amplitudes of $|u_y|$ under $\theta_2 = 60°$ were smaller than those under $\theta_2 = 0°$, and the responses in $|u_y|$ along the canyon surface were smoother. However, reflective waves from the boundary of the soft layer generated an oscillation with larger wavelength in the shadow zone, which was likely due to the canyon-decay effect and the thickness effect [22] associated with the soft layer in Fig. 2.

Figures 5 and 6 present 3-D plots illustrating surface responses (i.e., near and at the canyon surface) as a function of frequency in the seven selected locations shown in Fig. 7a, the details of which are listed in

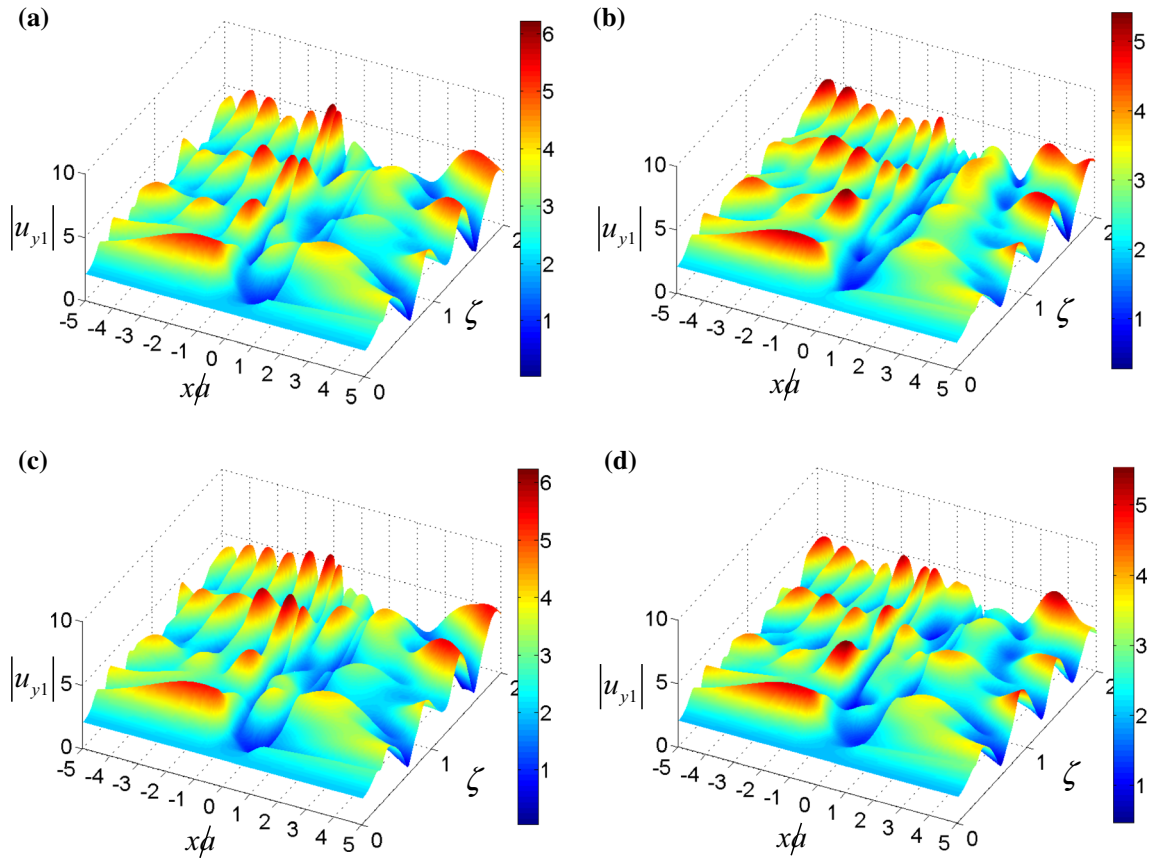

Fig. 6 Variations in $|u_{y1}|$ on free surface of single-layer half-plane where $\theta_2 = 60°$ with $-5 \le x/a \le 5$ in four types of canyon: (**a**) Case 1; (**b**) Case 2; (**c**) Case 3; and (**d**) Case 4

Table 4 Information related to specific locations

		x/a	z/a	Slope
$P_1(P_7)$		−2.0(2.0)	0.00	0.00
$P_2(P_6)$		−1.0(1.0)	0.00	none
$P_3(P_5)$	Case 1	−0.488(0.488)	0.873	±0.56
	Case 2	−0.5(0.5)	0.5	±1.00
	Case 3	−0.5(0.5)	1.0	none
	Case 4	−0.508(0.508)	0.647	±0.44
P_4	Case 1	0.0	1.00	0.00
	Case 2		1.00	none
	Case 3		1.00	0.00
	Case 4		0.75	0.00

Table 4. It was observed that the slopes at the canyon surface were discontinuous at SDCPs, such as P_4 in Case 2, $P_3(P_5)$ in Case 3, and $P_2(P_6)$ in all cases. The surface responses versus ζ are presented in the form of displacement spectra, which could be treated as transfer functions, as shown in Fig. 7b–e and Fig. 8 under various incident angles ($\theta_2 = 0°$, and 60°). The transfer functions are indicated by four curves: solid blue line (Case 1), dashed red line (Case 2), dash-dot black line (Case 3), dash-dot pink line (Case 4), and dashed light-blue line (single-layer half-space). Due the symmetric nature of the system, the transfer functions in Fig. 7b–d are presented at only four locations.

As shown in Figs. 7b–e and 8, the patterns in Cases 1 and 3 were similar at locations $P_1(P_7)$, $P_2(P_6)$, and P_4 under $\theta_2 = 0°$ and 60°. These similarities can be attributed to similarities in the areas and shapes of these two cases. We observed similar patterns of Cases 2 and 4 at locations P_1 and P_2 under $\theta_2 = 0°$ and 60°. The response patterns were affected by the area of the canyon (i.e., canyon-area effect). Thus, the four cases could

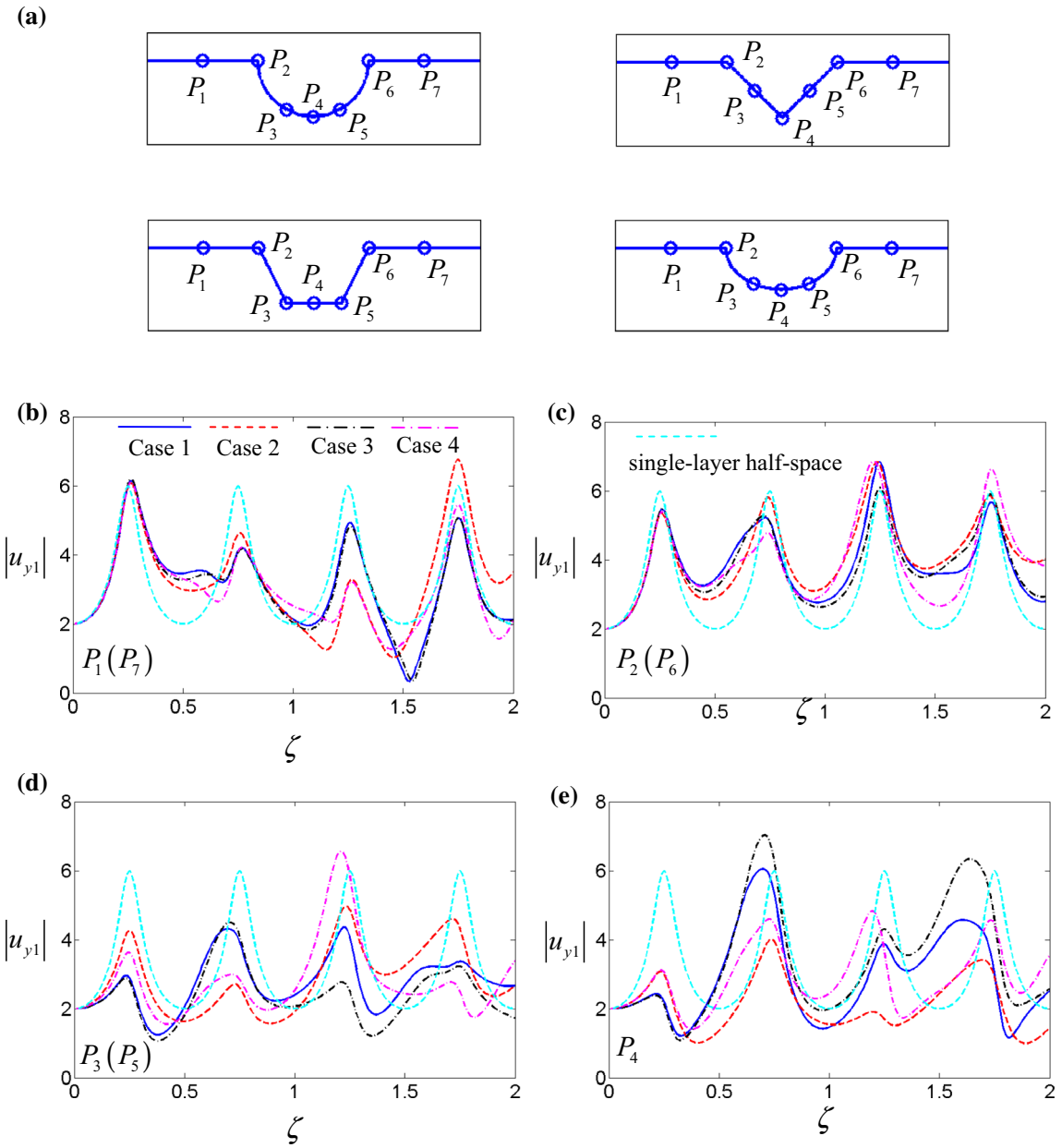

Fig. 7 (**a**) Specific locations on canyon surface and transfer functions in four cases with ζ under $\theta_2 = 0°$ at (**b**) $P_1(P_7)$; (**c**) P_2 (P_6); (**d**) $P_3(P_5)$; and (**e**) P_4

be divided into two groups: Group 1 (Cases 1 and 3) and Group 2 (Cases 2 and 4). The canyon-area effect weakened the responses under ζ_2^M in the illuminated zone where $\theta_2 = 0°$, as shown in Fig. 7b. However, the responses under ζ_1^M, ζ_3^M and ζ_4^M were more pronounced under $\theta_2 = 60°$, as shown in Fig. 8a. The canyon-area effect increased the transfer function in the left canyon corner of the canyon, near the wave fronts shown in Figs. 7c and 8b.

As shown in Table 4, position x/a was closer to boundary L at location P_3 (P_5), indicating that under the effects of a thinner soft layer, the transfer functions differed considerably from the surface responses (i.e., P_1 and P_7), particularly at higher RFs, as shown in Figs. 7d and 8c and e. Note that the regular RFs of the single-layer half-space were disturbed under $\theta_2 = 60°$, particularly in location P_3 in Case 2. Furthermore, the flat canyon boundary generated responses $\left|u_{y1}\right| \approx 2.0$ under an oblique incident angle within a range

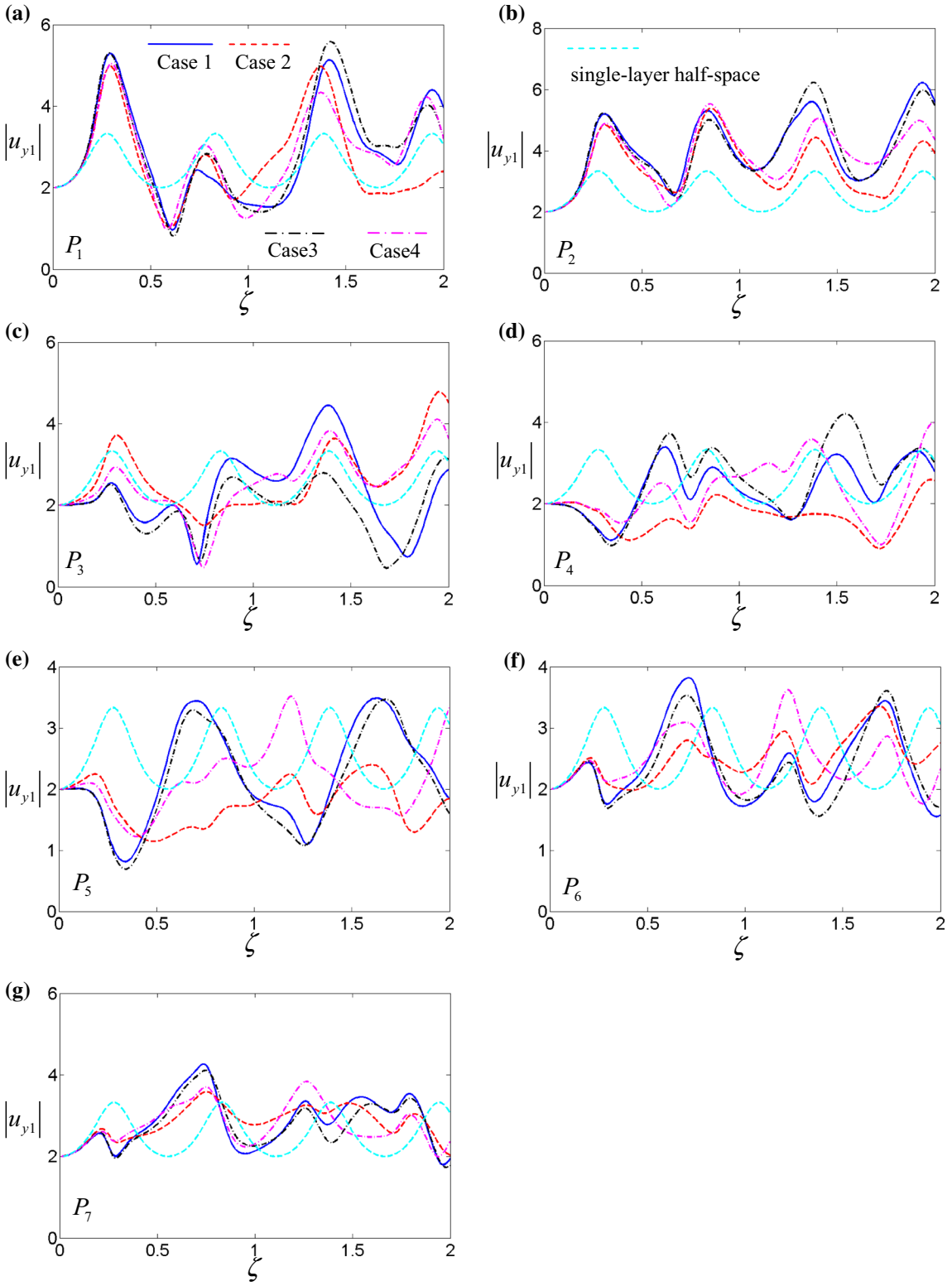

Fig. 8 Transfer functions in four cases with ζ under $\theta_2 = 60°$ at (**a**) P_1; (**b**) P_2; (**c**) P_3; (**d**) P_4; (**e**) P_5; (**f**) P_6; and (**g**) P_7

of $0.8 \leq \zeta \leq 1.3$, as shown in Fig. 8c. The canyon-area effect thoroughly disturbed the transfer function at location P_5, as shown in Fig. 8e. Note that we observed a similar pattern for Group 1 in Fig. 8a–e; however, the value of ζ_3^M shifted forward in Group 2, but shifted backward in Group 1, as shown in Fig. 8e.

We considered the transfer function at location P_4 at the bottom of the canyon, which is closest to layered boundary L, corresponding to the thinnest region of the soft layer in Figs. 7e and 8d. The wave front that reached P_4 generated creeping waves along the canyon surface toward each corner of the canyon. This had the effect of splitting the carrying energy and thereby decreasing the strength of responses within the region adjacent to ζ_1^M. In Case 3, the flat surface at the location of P_4 resulted $\left|u_{y1}\right|$ responses closer to those of the half-space under $\theta_2 = 0°$ as $\zeta > \zeta_1^M$, as shown in Fig. 7e. In Case 2, P_4 occurred at an SDCP, such that the corresponding responses were markedly lower when $\theta_2 = 60°$, as shown in Fig. 8d.

Figure 8f and g illustrates the transfer functions in the right corner of the canyon (i.e., P_6) and shadow zone (i.e., P_7) under $\theta_2 = 60°$. The shielding effect of the canyon reduced the amplitudes of $\left|u_{y1}\right|$ under ζ_1^M; however, the range of $\left|u_{y1}\right|$ values was closer to that of a single-layer half-space, where $\zeta > \zeta_1^M$. In all cases, the *RF*s of ζ_2^M to ζ_4^M shifted forward at location P_6, and a relatively clear *RF* (ζ_2^M) existed only at P_7, as shown in Fig. 8f and (g), respectively.

3.4 Site effects of the canyon in a half-space and single-layer half-space under specific ζ

To analyze the responses of *RF*s on the free surface, we plotted Figs. 9 and 10 with specific frequencies versus positions. We selected four dimensionless frequencies (0.25, 0.75, 1.35, and 1.64) under $\theta_2 = 0°$, as shown in Fig. 9. We also selected another four dimensionless frequencies (0.28, 0.71, 1.39, and 1.94) under $\theta_2 = 60°$, as shown in Fig. 10. Most of these specific frequencies were based on the *RF*s in Table 1. Nonetheless, some of the *RF*s were selected from the transfer functions shown in Figs. 7 and 8, including $\zeta = 1.35$, and 1.64 (Fig. 9), and $\zeta = 0.71$ (Fig. 10). The transfer functions were illustrated using four curves: solid blue line (Case 1), dashed red line (Case 2), dash-dot black line (Case 3), dash-dot pink line (Case 4), and dashed light-blue line (indicating responses under specific ζ values within a single-layer half-space).

With the exception of Fig. 10c, Figs. 9 and 10 confirm that the surface response patterns were indeed altered by canyon-area effect. Under $\theta_2 = 0°$ (Fig. 9), the responses in Group 2 (Cases 2 and 4) along canyon surfaces (particularly in the central region of the canyon) were far smaller than those in Group 1 (Cases 1 and 3). Overall, the canyon-decay effect weakened responses along the surface of canyon, except for Group 1 at higher frequencies. Responses in illuminated zone and shadow zone fluctuated with displacement values at the free surface of the single-layer half-space (i.e., $\left|u_{y1}^f\right|$). This resulted in more pronounced responses at the canyon surface, but weaker responses in the free half-space under vertical incident waves. Under $\theta_2 = 60°$, canyon-area effect observed in the illuminated zone was similar to those at the canyon surface, as shown in Fig. 10a, b and d. However, under specific ζ values, the canyon-decay effect was not observed. These gaps included all cases under $\zeta = 0.71$ (Fig. 10b), Case 4 under $\zeta = 1.39$ (Fig. 10c), and Group 1 under $\zeta = 1.94$(Fig. 10d). We speculate that the thickness effect destroyed the canyon-decay effect. Thus, under oblique incident waves, reflective waves with a shorter wavelength (i.e., higher frequency) generated a constructive interference at the surface of the canyon and within the shadow zone, as shown in Fig. 10.

As shown in Figs. 11 and 12, we examined the thickness effect due to the soft layer by focusing on ζ in Cases 1 to 4 and Cases I to IV under $\theta_2 = 0°$ and $\theta_2 = 60°$. The results for Cases 1 to 4 are indicated by the solid blue line, and the results for Cases I to IV are indicated by the dashed red line. As shown in Fig. 11, the patterns for Cases 1 to 4 were similar to those for Cases I to IV. This is an indication that the soft layer generated more pronounced responses at the surface under vertical incident waves. However, the responses in Cases 1 to 4 were similar to those in Cases I to IV under relatively high ζ values (such as 1.35 and 1.64), as shown in Fig. 11c, d. Thus, the short wavelengths transformed the soft layer into a half-space. In Fig. 12, the thickness effect was obviously under an oblique incident angle such as $\theta_1 = 25.66°$. We therefore added a dash-dot black line indicating the results of Cases I to IV with an incident angle of 30° in the half-space. We can see that the patterns of Cases 1 to 4 ($\theta_2 = 60°$) were similar to those for Cases I to IV with an incident angle of 30°. This is a clear indication that the thickness effect brought the incident angle closer to the vertical direction.

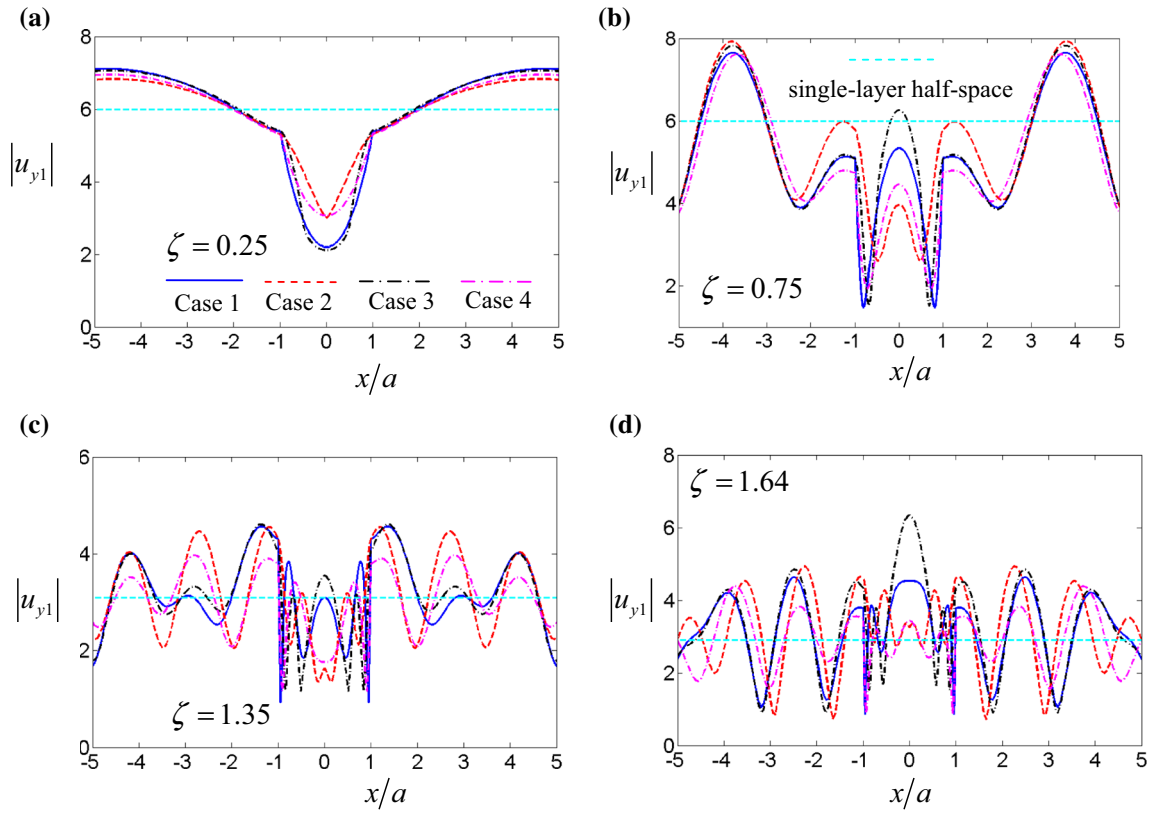

Fig. 9 Variations in $|u_{y1}|$ in Cases 1 to 4 where $-5 \le x/a \le 5$ and $\theta_2 = 0°$ under (**a**) $\zeta = 0.25$; (**b**) $\zeta = 0.75$; (**c**) $\zeta = 1.35$; and (**d**)$\zeta = 1.64$

4 Results of displacement in the time domain

4.1 Ricker wavelet in the time domain and frequency domain

Responses in the time domain were derived from results obtained in the frequency domain results using the inverse fast Fourier transform (FFT) algorithm. The incident time signal was a Ricker wavelet as follows:

$$u_{Ric}(t) = \left[2\pi^2 f_c^2 (t - t_s)^2 - 1\right] \exp\left[-\pi^2 f_c^2 (t - t_s)^2\right] \tag{6}$$

where f_c indicates the characteristic frequency of the wavelet and t_s is the peak amplitude of the wavelet in the time domain. The Ricker parameters were set as $t_s = 0.0sec$ and $f_c = 0.5Hz$, and we considered that these values were able to emphasize the effect of a canyon embedded within single-layer half-space. The response in the time domain and its corresponding Fourier amplitude spectrum are presented in Fig. 13. The maximum amplitude of displacement in the time domain was 1.0, such that the maximum amplitude at the free surface of the half-space was 2.0. The half-width of the canyon (a) was set 1.0 km, and the depth of the soft layer (H) was set as 2.0 km. The shear wave velocities in the soft layer and half-space were $C_{s1} = 1.0km/sec$ and $C_{s2} = 2.0km/sec$, respectively. The canyon depths are listed in Table 3. We selected a reference point in the half-space (or single-layer half-space) under $\theta_2 = 0°$ and 60°, as shown in Fig. 14. The time required for the peak of $u_{Ric}(t)$ to arrive at original point O (i.e., $(x, z) = (0, 0)$) from the reference point was 6 s. The number of calculated frequencies was 96, ranging from 0.00 to 1.52 at intervals of 0.016, and the time window was set at 15 s.

4.2 Time domain responses of the canyon surface in half-space and single-layer half-space

In this section, we consider time domain responses (i.e., $u_y(t)$) in the specific locations discussed in Sect. 3.2. Figures 15 and 16, respectively, present the responses in these locations under $\theta_2 = 0°$ and 60°. The results

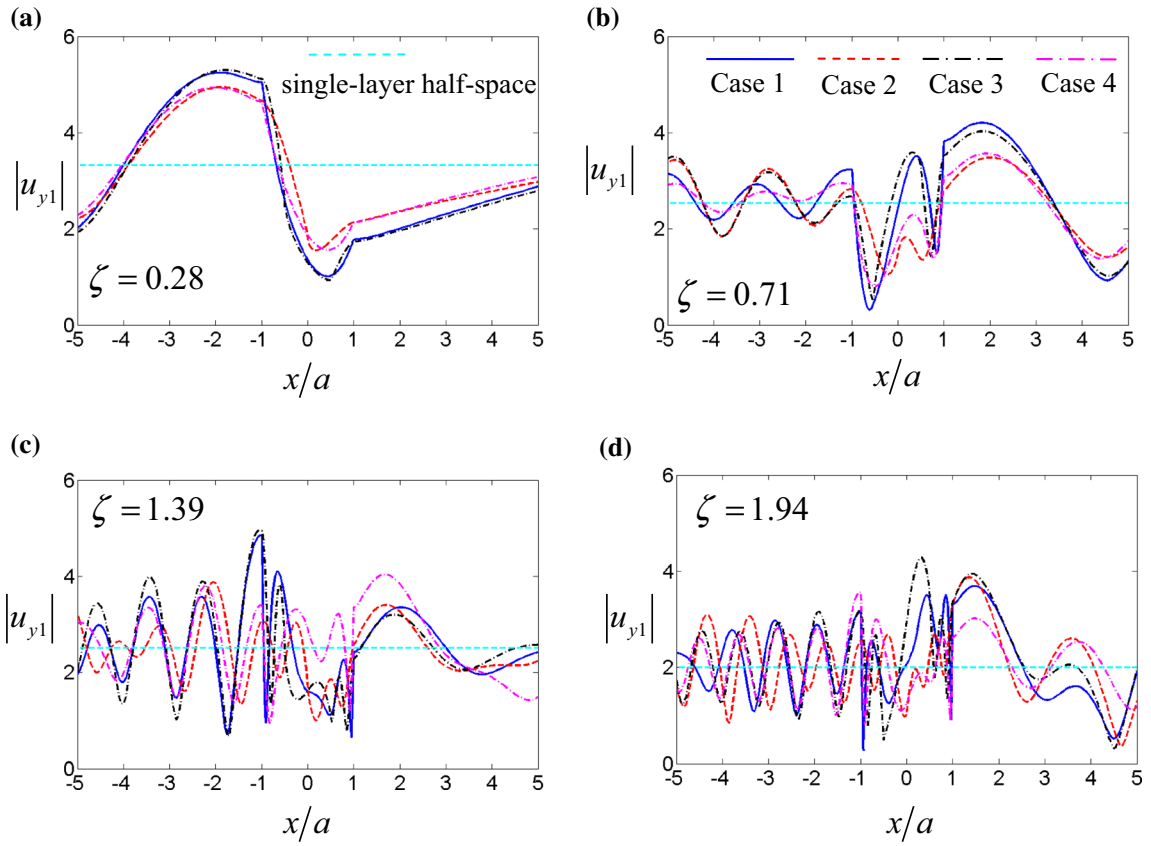

Fig. 10 Variations in $|u_{y1}|$ in Cases 1 to 4 where $-5 \le x/a \le 5$ and $\theta_2 = 60°$ under (**a**) $\zeta = 0.28$; (**b**) $\zeta = 0.71$; (**c**) $\zeta = 1.39$; and (**d**) $\zeta = 1.94$

for Cases 1 to 4 are indicated by the solid blue line, and those of Cases I to IV are indicated by the dashed red line. As this analysis focused on symmetric canyons impinged by vertical incident wave, Fig. 15 presents only four locations. Figures 15a–d and 16a–d, respectively, present the semicircular, triangular, trapezoid, and shallow semi-elliptical canyons.

As shown in Fig. 15, larger responses occurred in Cases 1 to 4 under the effect of a soft layer on hard bedrock. The maximum absolute value of displacement (i.e., $|u_y(t)|$) occurred in the corner of the canyon (i.e., P_2 and P_6), as shown in Fig. 15a2–d2. We also observed that $u_y(t)$ at the surface of the canyon (including the corner) was the reverse of the pattern of $u_{Ric}(t)$ under the effects of the canyon surface. Note that in each location, the arrival times of the peaks in $u_y(t)$ (i.e., t_a) in Cases 1 to 4 were similar to those in Cases I to IV, under the effects of the first wave front. For example, $t_a = 6\ sec$ at locations P_1 (P_7) and P_2 (P_6) (see Fig. 15a1–d1 and a2–d2, $t_a = 5.5\ sec$ at locations P_3 (P_5) (see Fig. 15a3–d3) and $t_a = 5\ sec$ at location P_4 (see Fig. 15a4–d4). These results could be easily derived from Fig. 14a using ray theory. Note also that the responses observed in the time domain for Cases 1 and 4 were identical to the patterns for Cases I and IV under a vertical incident angle, except for the ratio of amplitude values. Note that the response durations in Case 2 and 3 were relatively long (15 s), as indicated by a peak at roughly 10 s in locations P_1 (P_7) and P_2 (P_6), as shown in Fig. 15b1–b2 and c1–c2. Note also that the time interval between the two peaks (4 s) was equal to the value of $2H/C_{s1}$. This resulted in a reflective wave from boundary L. A shorter distance between location P_3 (P_5) or P_4 and the position of first wave front produced a series of rapid oscillation responses, as shown in Fig. 15 a3–d3 and a4–d4.

As shown in Fig. 16a2–d2, the larger responses in Cases 1 to 4 generated maximum values of $|u_y(t)|$ in the corner of the canyon near the wave front (i.e., P_2). We also observed the reverse pattern of $u_{Ric}(t)$ in the canyon corners and along the canyon surface (i.e., P_2 to P_6), except in flat locations (i.e., P_1 and P_7). Arrival time t_a was similar in Cases 1 to 4: P_1 (5.1 s), P_2 (5.5 s), P_6 (6.4 s), and P_7 (6.9 s). Arrival time t_a was also similar in Cases I to IV: P_1 (4.3 s), P_2 (5.1 s), P_6 (7.1 s), and P_7 (7.7 s). These results could also be

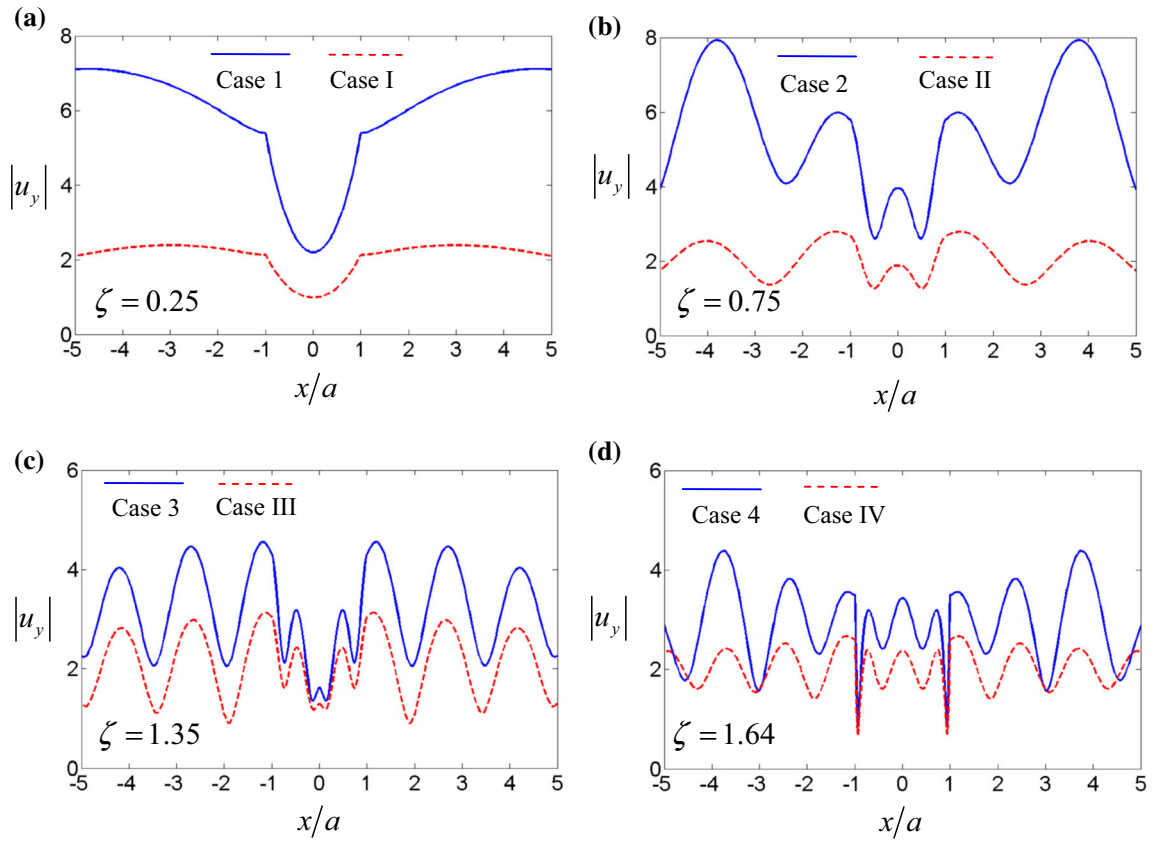

Fig. 11 Variations in $|u_y|$ where $-5 \le x/a \le 5$ and $\theta_2 = 0°$: (**a**) Case 1 versus Case I under $\zeta = 0.25$; (**b**) Case 2 versus Case II under $\zeta = 0.75$; (**c**) Case 3 versus Case III under $\zeta = 1.35$; and (**d**) Case 4 versus Case IV under $\zeta = 1.64$

derived using ray theory, as shown in Fig. 14b. As shown in Fig. 14b, we calculated distance $D \approx 4.3km$ in the half-space, as well as $D_1 \approx 5.9km$ and $D_2 \approx 2.2km$ in the single-layer half-space in order to derive the arrival time at location P_1. Note, however, that this did not allow us to obtain the results in other locations, due to wave front attacking the canyon surface to generate creeping waves. Thus, the arrival times were faster in the illuminated zone (i.e., P_1) and in the left corner (i.e., P_2), as shown in Fig. 16a1–d1 and a2–d2. The arrival times were slower in the right corner (i.e., P_6) and in the shadow zone (i.e., P_7), as shown in Fig. 16a6–d6 and a7–d7. At location P_3, arrival times were similar in all the cases (about 5 s). Beyond location P_3, arrival times differed according to case in locations P_4 and P_5, due to the shape of the canyon. At location P_4, the arrival times in Cases I to IV were slower than those in Cases 1 to 4. As mentioned above, it was easier to obtain this information under an oblique incident angle, due to the fact that the thickness effect did not play a pronounced role in cases of vertical incident waves.

The three-dimensional (3-D) illustrations in Figs. 17 and 18 illustrate variations in the responses of $u_y(t)$ as functions of position (i.e., x/a, ranging from -5.0 to 5.0) and time (t, ranging from 0.0 to 15.0). Figures 17 and 18a–d present Cases 1 to 4, respectively, under $\theta_2 = 0°$ and 60°. Based on the parameters of the Ricker wavelet, the arrival time to the free surface of flat plane was set at 6 s after the first wave front. As shown in Fig. 17, the shapes of the canyon could be detected prior to 6 s under the effect of wave propagation. The reverse patterns of $u_y(t)$ are indicated by the red color in Fig. 17 along the surface of the canyon and in the canyon corners. Due to the symmetric shapes of the canyon and vertical incident angle, the responses of $u_y(t)$ in the illuminated zone ($x/a \le -1.0$) and shadow zone ($x/a \ge -1.0$) were precisely the same. The slope of the dashed red line shown in Fig. 17 indicates the wave speed on the flat free surface which was equal to $C_{s1} = 1km/sec$. However, the slope of dashed light-blue line suggests that the wave speed along the canyon surface (i.e., $0.6km/sec$) was lower than C_{s1}. The dashed black lines in Fig. 17b, c also indicate the obvious reflective wave from boundary L in Cases 2 and 3, which was largely obscured in Cases 1 and 4, as discussed above.

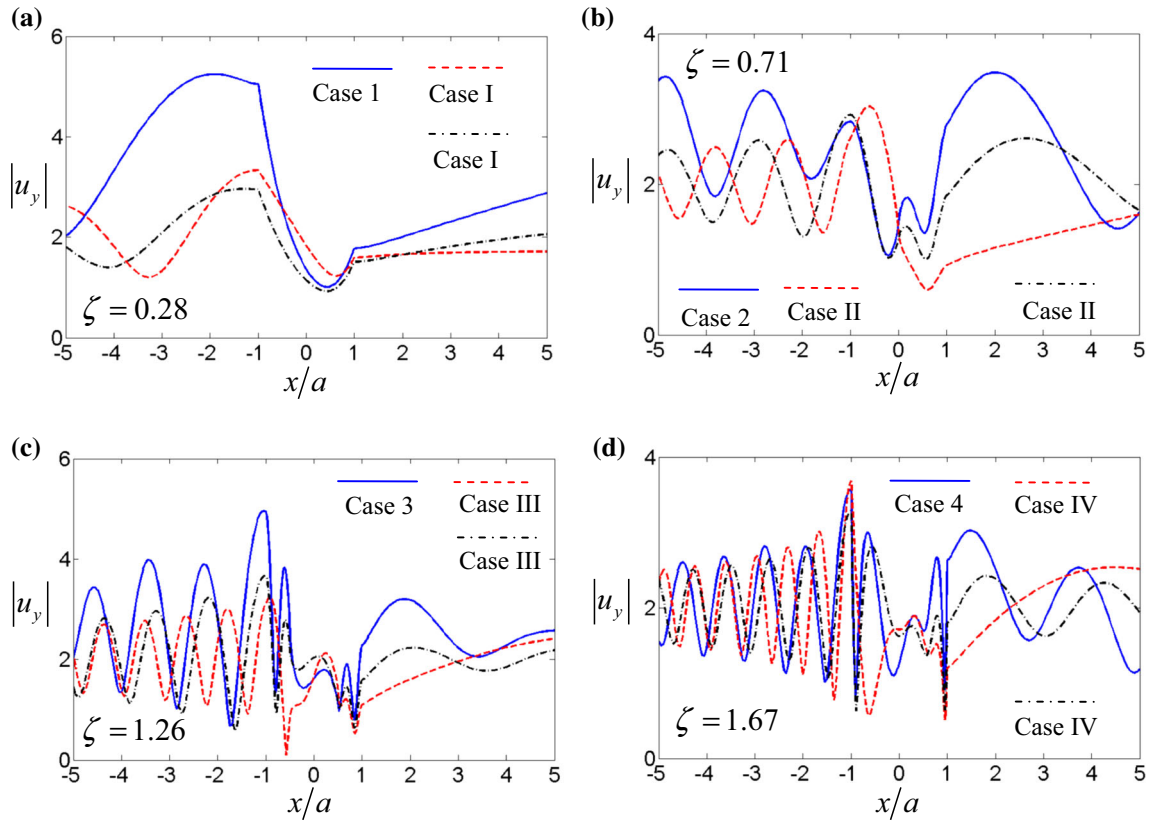

Fig. 12 Variations in $|u_y|$ where $-5 \le x/a \le 5$ and $\theta_2 = 60°$: (**a**) Case 1 versus Case I under $\zeta = 0.28$; (**b**) Case 2 versus Case II under $\zeta = 0.71$; (**c**) Case 3 versus Case III under $\zeta = 1.26$; and (**d**) Case 4 versus Case IV under $\zeta = 1.67$ (dash-dot black line indicates results of Cases I to IV where $\theta_2 = 30°$)

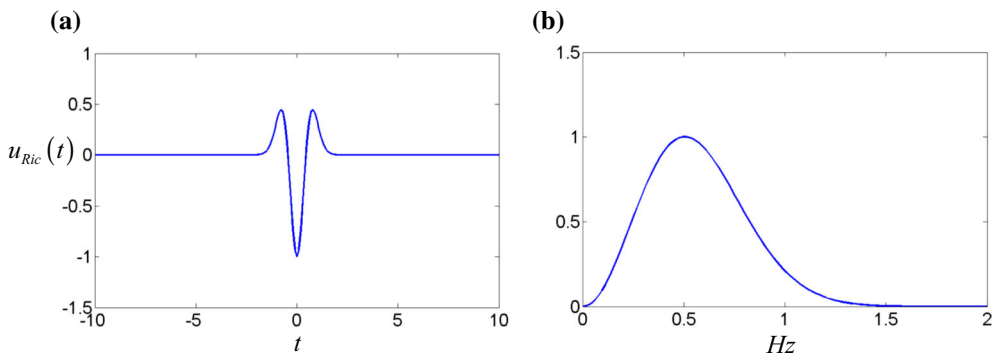

Fig. 13 Ricker wavelet response in (**a**) the time domain and (**b**) the frequency domain

As shown by the travel time curves in Fig. 18, the canyon shapes were twisted under the effect of oblique incident angle $\theta_2 = 60°$. The angle of the solid black line in Fig. 18a is 23.16°, which is close to refractive angle $\theta_1 = 25.66°$. The apparent speed on the free surface was equal to $C_{s1}/\sin\theta_1$ (about $2.33 km/sec$), which was faster than C_{s1}. Thus, it appears that the thickness effect generated a faster apparent speed on the free surface. The slope of the dashed red line in the illuminated zone indicates that the wave speed was equal to C_{s1}. The slope of the dashed and dash-dot light-blue lines, respectively, indicates wave speeds of $0.6 km/sec$ and $0.48 km/sec$ along the canyon surface. The slope of the dash-dot red line in the shadow zone indicates that the wave speed ($1.12 km/sec$) was greater than C_{s1}, resulting in faster reflective waves in the shadow zone. The dashed black line in Fig. 18b, c indicates that the boundary effect due to L was clear only in Cases 2 and 3.

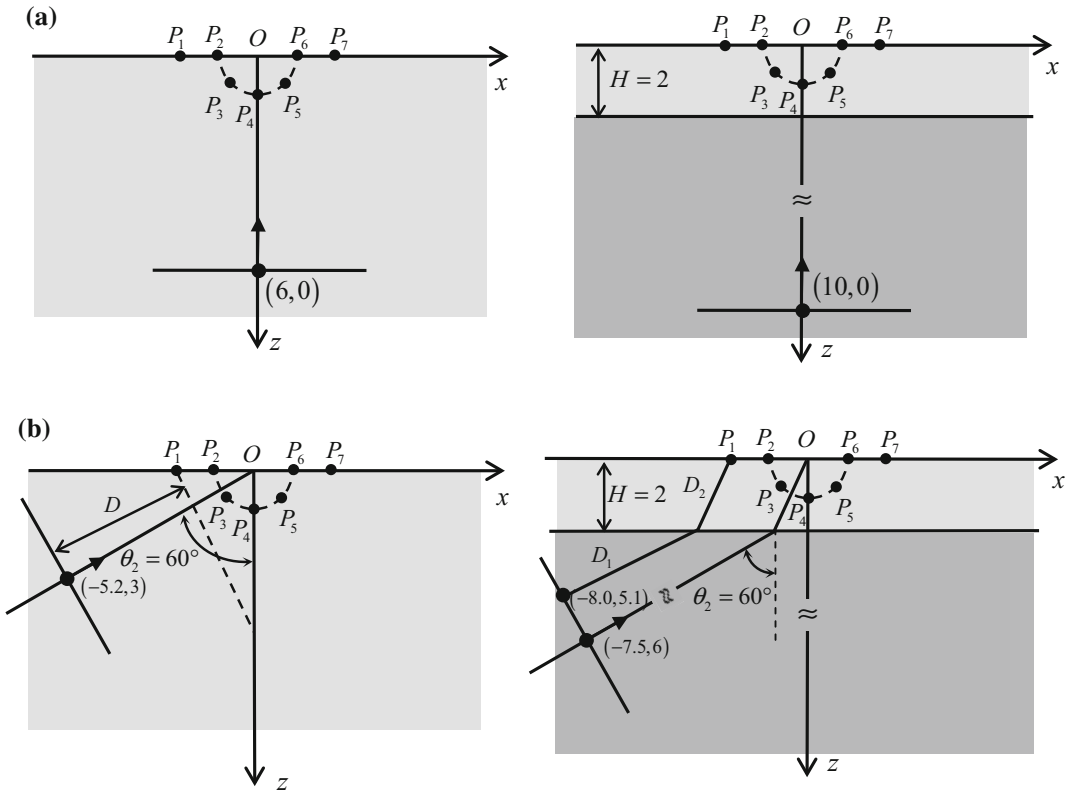

Fig. 14 First wave front at specific locations in half-space and single-layer half-space where (**a**) $\theta_2 = 0°$ and (**b**) $\theta_2 = 60°$

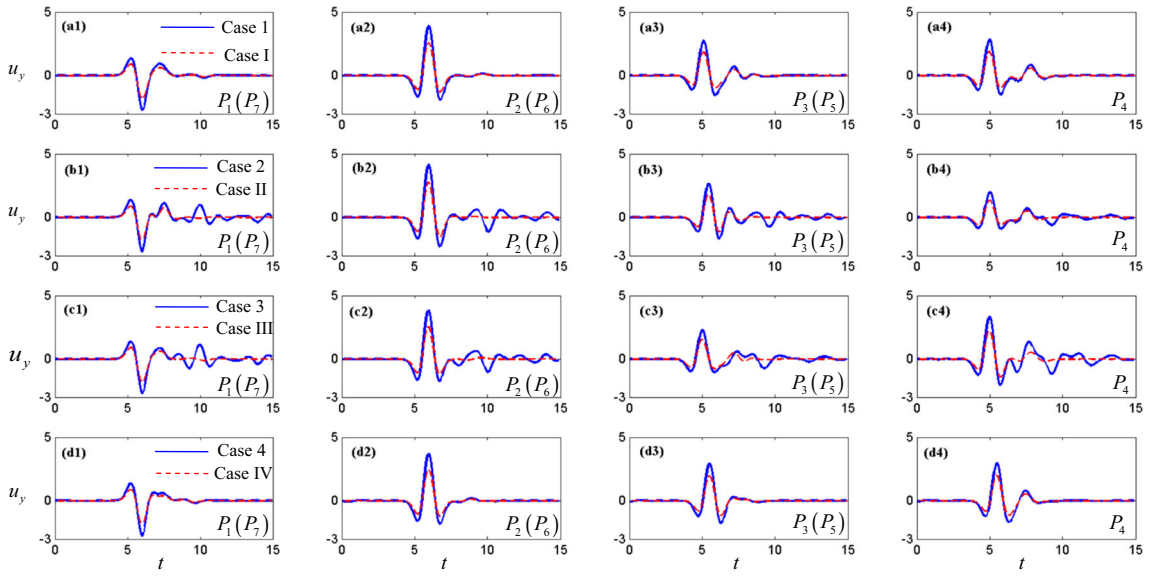

Fig. 15 Variations in $u_y(t)$ at specific locations where $\theta_2 = 0°$: (**a**) Case 1 versus Case I; (**b**) Case 2 versus Case II; (**c**) Case 3 versus Case III; and (**d**) Case 4 versus Case IV

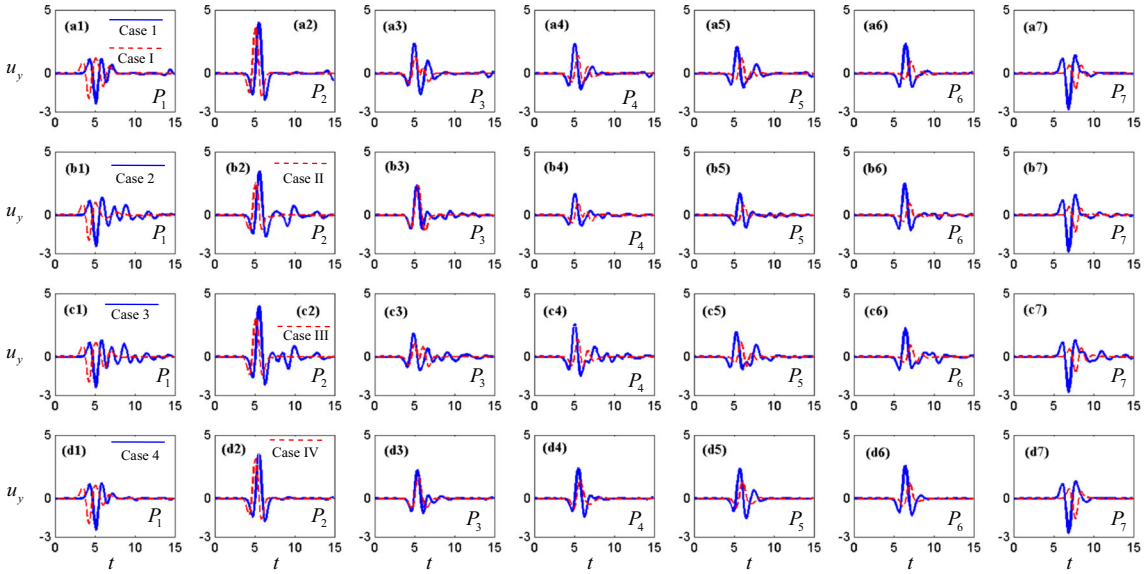

Fig. 16 Variations in $u_y(t)$ at specific locations where $\theta_2 = 60°$: (**a**) Case 1 versus Case I; (**b**) Case 2 versus Case II; (**c**) Case 3 versus Case III; and (**d**) Case 4 versus Case IV

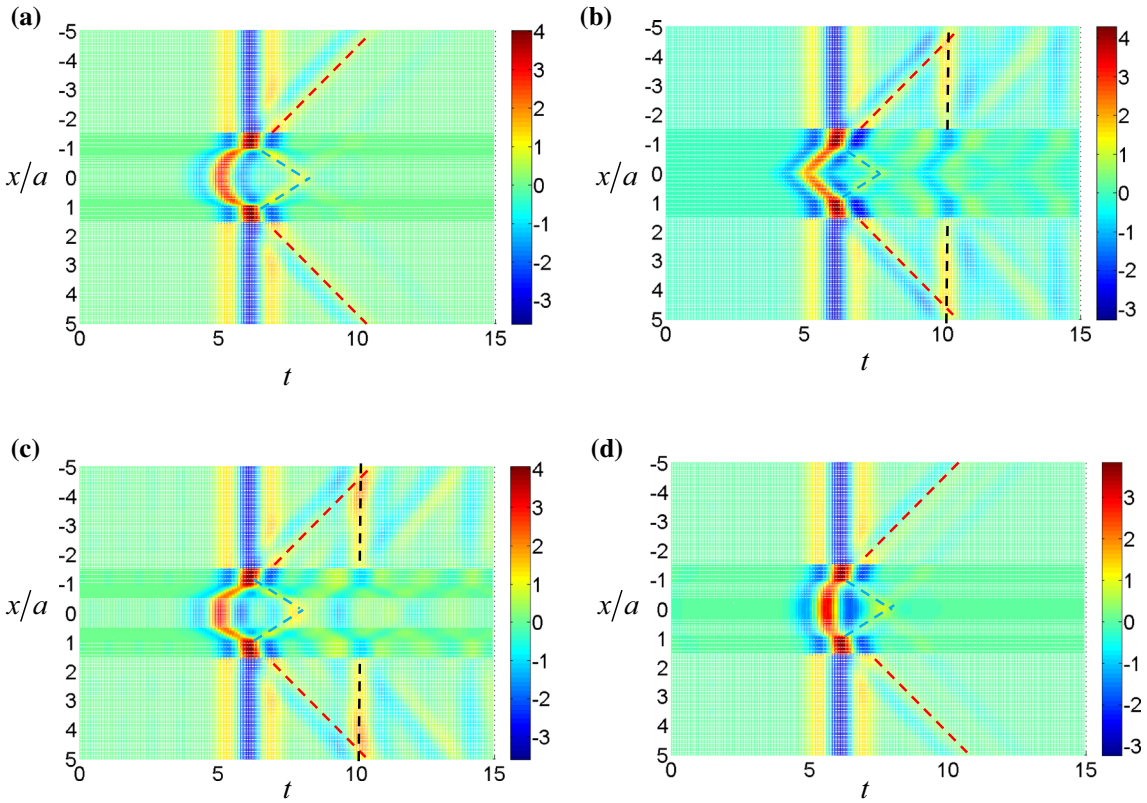

Fig. 17 Variations in $u_y(t)$ under $\theta_2 = 0°$ where $-5 \le x/a \le 5$ and $0 \le t \le 15$ on free surface of single-layer half-plane: (**a**) Case 1; (**b**) Case 2; (**c**) Case 3; and (**d**) Case 4

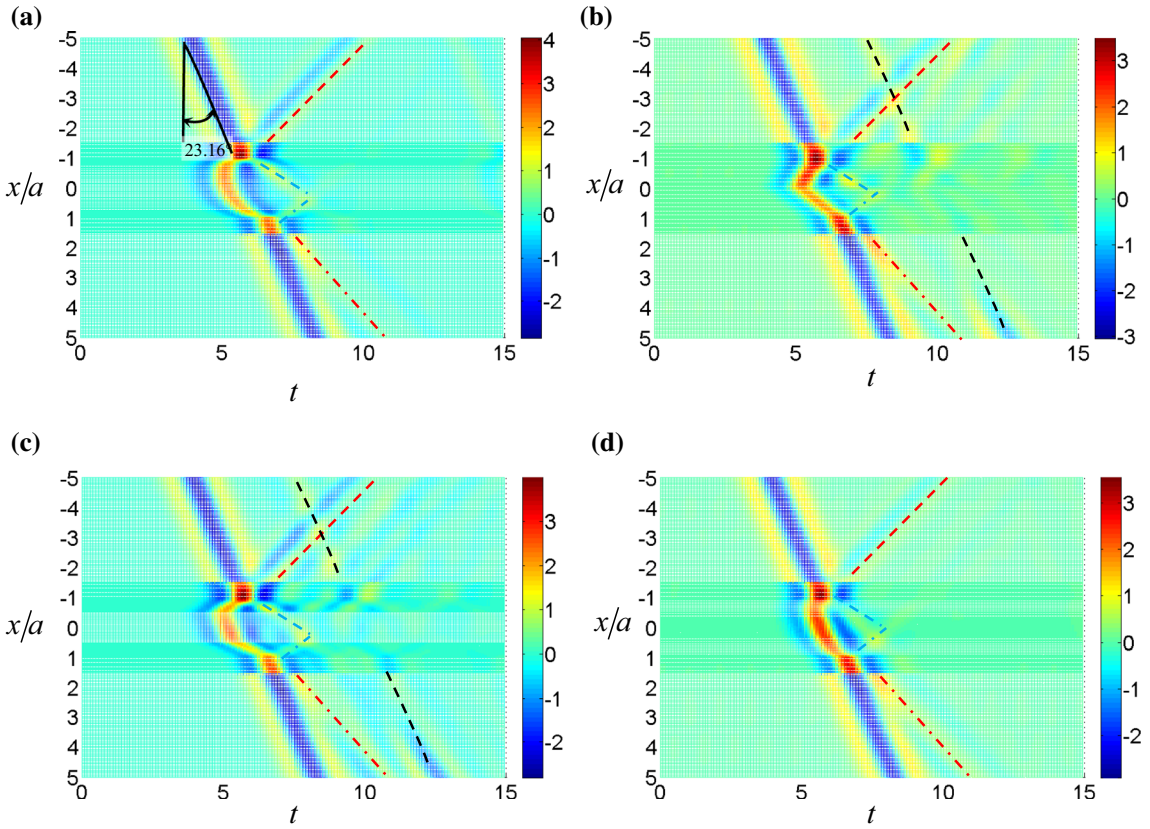

Fig. 18 Variations in $u_y(t)$ under $\theta_2 = 60^\circ$ with $-5 \leq x/a \leq 5$ and $0 \leq t \leq 15$ on the free surface of single-layer half-plane with (**a**) Case 1; (**b**) Case 2; (**c**) Case 3; and (**d**) Case 4

5 Conclusions

In this paper, we used a modified hybrid method combining FEM with a Lamb series to investigate the scattering of *SH* waves and the related site effects resulting from a symmetric canyon embedded in a single-layer half-space. Important points are as follows:

(1) To introduce the dimensionless frequency and the ratio of materials was helpful to simplify the discussion of scattering problem.
(2) The thickness effect generated by soft layer could enhance surface responses, bringing the incident angle toward vertical. This generated larger surface responses in Cases 1 to 4 under relatively low frequencies and produced responses similar to those of a half-space (i.e., Cases I to IV) under relatively high frequencies. In cases where the canyon shape included SDCPs, the flat surface of the canyon could bring the responses closer to those of flat free surface under thickness effect.
(3) We observed a canyon-decay effect and shielding effect resulting from the canyon topography. However, the thickness effect increased the complexity of the responses.
(4) Similar patterns in the response spectrum can be attributed to similar areas. For example, *RF*s in Group 2 (smaller area) shifted forward and *RF*s in Group 1 (larger area) shifted backward.
(5) The effects on $u_y(t)$ at the canyon surface (such as locations P_3, P_4, and P_5) and in the corners (such as location P_2, and P_6) represented a reversal of the patterns (as shown in Figs. 15 and 16) related to incident waves (e.g., $u_{Ric}(t)$, as shown in Fig. 13a), which were affected by the existing canyon.
(6) The arrival time of $u_y(t)$ in some locations (such as the illuminated zone) could be obtained using ray theory. However, the arrival time in locations along the canyon (and shadow zone) could not be discerned under the creeping waves.
(7) A soft layer in combination with an oblique incident angle could enhance the speed of apparent waves, such that the time of arrival at the canyon (and in shadow zone) in Cases 1 to 4 occurred sooner than in Cases I to IV.

(8) Calculations of high-frequency response were the limitations of this modified hybrid method. (For example, the dimensionless frequency was limited to 1.5 [23].) However, it was still useful to obtain the response under relative low dimensionless frequencies (i.e., the larger H or λ_1).

Embedding a canyon in a layered half-space proved effectively in elucidating site effects. The modified hybrid method proposed in this paper made it possible to systematically study the scattering of anti-plane *SH* incident waves induced by a complex topography embedded within a single-layer half-space.

Acknowledgements The authors would like to thank the Ministry of Science and Technology, Taiwan R. O. C., for financially supporting this research under Contract No. MOST 111-2221-E-020-015-.

Data availability The data and code relating to this work may be provided on personal request.

Appendix 1

The single-layer half-space in Fig. 19 was disturbed by a virtual load acting at the original point:

$$\left(\sigma^s_{zy1}\right)_m = -\mu_1 \delta^{(m)}(x), \text{ at } (x, z) = (0, 0) \tag{A-1}$$

where $\delta(x)$ is the Dirac delta function. Symbol $\delta^{(m)}$ represents the m-th derivative of $\delta(x)$ with respect to x. The virtual load in Eq. (A-1) is one type of Lamb load.

The displacements generated by the disturbance satisfied the governing equation as well as the corresponding boundary conditions as follows:

$$\frac{\partial^2 u^s_{yj}}{\partial x^2} + \frac{\partial^2 u^s_{yj}}{\partial z^2} + k^2_{sj} u^s_{yj} = 0; \ j = 1 \ , \ 2 \tag{A-2}$$

$$\left(\sigma^s_{zy1}\right)_m = \left(\sigma^s_{zy2}\right)_m, \text{ at } z = H \tag{A-3}$$

$$\left(u^s_{y1}\right)_m = \left(u^s_{y2}\right)_m, \text{ at } z = H \tag{A-4}$$

where superscript s refers to displacements or stresses in the scattering field. The solutions to Eq. (A-2) are series functions, based on the given value of m, which can be obtained using the following boundary conditions: (1) traction free at the free surface except at the original point, as shown in Eqs. (1) and (2) continuous displacements and tractions along interface L, as shown in Eqs. (A-3) and (A-4). The series functions also satisfied the radiation condition, which means that the energy of waves decayed after propagating over an extended distance. This makes it possible to express the displacements $\left(u^s_{yj}\right)_m$, stresses including $\left(\sigma^s_{xyj}\right)_m$ and $\left(\sigma^s_{zyj}\right)_m$, as well as tractions $\left(t^s_{yj}\right)_m$ in the scattered field, as follows:

$$\left(u^s_{y1}\right)_m = \frac{1}{2\pi}\int_{-\infty}^{\infty} A^1_U e^{-\nu'_1(H-z)-ikx} dk + \frac{1}{2\pi}\int_{-\infty}^{\infty} A^1_D e^{-\nu'_1 z - ikx} dk \tag{A=5a}$$

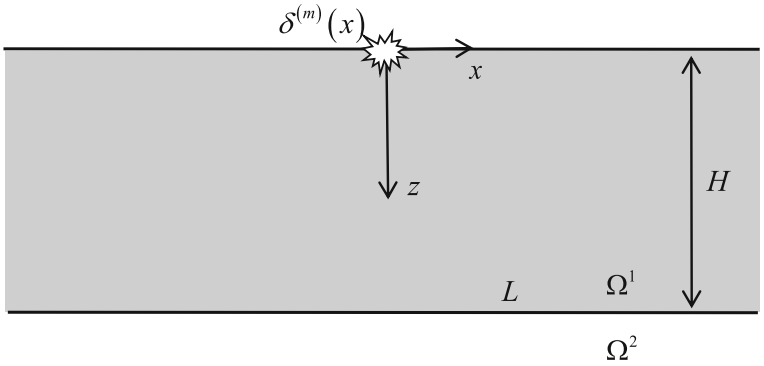

Fig. 19 Schematic diagram showing single-layer half-space under excitation via surface loading

$$\left(u^s_{y2}\right)_m = \frac{1}{2\pi}\int_{-\infty}^{\infty} A^2_D e^{-\nu'_2(z-H)-ikx}dk \tag{A-5b}$$

$$\nu'_j = \sqrt{k^2 - k^2_{sj}}, \qquad j = 1\ ,\ 2 \tag{A-5c}$$

$$A^1_D = \frac{1}{1 - R^{12}_D e^{-2\nu'_1 H}}\frac{(-\mathrm{i}k)^n}{\nu'_1};\ A^1_U = R^{12}_D A^1_D;\ A^2_D = T^{12}_D A^1_D \tag{A=5d}$$

$$R^{12}_D = \frac{\mu_1\nu'_1 - \mu_2\nu'_2}{\mu_1\nu'_1 + \mu_2\nu'_2}e^{-\nu'_1 H};\ T^{12}_D = \frac{2\mu_1\nu'_1}{\mu_1\nu'_1 + \mu_2\nu'_2}e^{-\nu'_1 H} \tag{A-5e}$$

and

$$\left(\sigma^s_{xyj}\right)_m = \mu_j\frac{\partial}{\partial x}\left(u^s_{yj}\right)_m;\ \left(\sigma^s_{zyj}\right)_m = \mu_j\frac{\partial}{\partial z}\left(u^s_{yj}\right)_m \tag{A-6a}$$

$$\left(t^s_{yj}\right)_m = \left(\sigma^s_{xyj}\right)_m n_x + \left(\sigma^s_{zyj}\right)_m n_z;\ j = 1,\ 2. \tag{A-6b}$$

Note that $\left(u^s_{yj}\right)_m$ is expressed using the integral form, as shown in Eq. (A-5a) or Eq. (A-5b). It can be obtained using the modified steepest descent method [37].

References

1. Trifunac, M.D.: Scattering of plane SH waves by a semi-cylindrical canyon. Earthq. Eng. Struct. Dyn. **1**, 267–281 (1973)
2. Shyu, W.S., Teng, T.J.: Hybrid method combines transfinite interpolation with series expansion to simulate the anti-plane response of a surface irregularity. J. Mech. **30**, 349–360 (2014)
3. Trifunac, M.D.: Surface motion of a semi-cylindrical alluvial valley for incident plane SH waves. Bull. Seismol. Soc. Am. **61**, 1755–1770 (1971)
4. Chen, J.T., Lee, J.W., Shyu, W.S.: SH-wave scattering by a semi-elliptical hill using a null-field boundary integral equation method and a hybrid method. Geophys. J. Int. **188**, 177–194 (2012)
5. Lee, V.W., Luo, H., Liang, J.: Antiplane (SH) waves diffraction by a semicircular cylindrical hill revisited: an improved analytic wave series solution. J. Eng. Mech. **132**, 1106–1114 (2006)
6. Liang, J., Fu, J.: Surface motion of a semi-elliptical hill for incident plane SH waves. Earthq. Sci. **24**, 447–462 (2011)
7. Huang, H.C., Chiu, H.C.: Canyon topography effects on ground motion at Feitsui damsite. Soil Dyn. Earthq. Eng. **18**, 87–99 (1999)
8. Tsaur, D.H., Chang, K.H.: An analytical approach for the scattering of SH waves by a symmetrical V-shaped canyon: shallow case. Geophys. J. Int. **174**, 255–264 (2008)
9. Guo, Y., Zhang, N., Li, D., Liu, H., Cai, Y., Wu, Y.: Effects of topographic amplification induced by a U-shaped canyon on seismic waves. Bull. Seismol. Soc. Am. **102**, 1748–1763 (2012)
10. Tsaur, D.H., Hsu, M.S.: SH-waves scattering from a partially filled semi-elliptic alluvial valley. Geophys. J. Int. **194**, 499–511 (2008)
11. Yuan, X., Liao, Z.P.: Surface motion of a cylindrical hill of circular-arc cross-section for incident SH waves. Soil Dyn. Earthq. Eng. **15**, 189–199 (1996)
12. Sánchez-Sesma, F.J., Rosenblueth, E.: Ground motion at canyons of arbitrary shape under incident SH waves. Earthq. Eng. Struct. Dyn. **7**, 441–450 (1979)
13. Sánchez-Sesma, F.J., Herrera, H., Aviles, J.: A boundary method for elastic wave diffraction: application to scattering of SH waves by surface irregularities. Bull. Seism. Soc. Am. **72**, 473–490 (1982)
14. Takemiya, H., Fujiwara, A.: SH-wave scattering and propagation analyses at irregular sites by time domain BEM. Bull. Seismol. Soc. Am. **84**, 1443–1455 (1994)
15. Chen, J.T., Chen, P.Y., Chen, C.T.: Surface motion of multiple alluvial valleys for incident plane SH-waves by using a semi-analytical approach. Soil Dynam. Earthq. Eng. **28**, 58–72 (2008)
16. Liu, J., Kausel, E., Liu, X.: Using pseudo-spectral method on curved grids for SH-wave modeling of irregular free-surface. J. Appl. Geophys. **140**, 42–51 (2017)
17. Gil-Zepeda, S.A., Montalvo-Arrieta, J.C., Vai, R., Sánchez-Sesma, F.J.: A hybrid indirect boundary element-discrete wave number method applied to simulate the seismic response of stratified alluvial valleys. Soil Dyn. Earthq. Eng. **23**, 77–86 (2003)
18. Shyu, W.S., Teng, T.J., Chou, C.S.: Determining anti-plane responses induced by oblique-truncated semicircular canyon using systematic hybrid method with mapping function. Soil Dyn. Earthq. Eng. **77**, 24–34 (2015)
19. Shyu, W.S., Teng, T.J., Chou, C.S.: Anti-plane response induced by an irregular alluvial valley using a hybrid method with modified transfinite interpolation. Soil Dyn. Earthq. Eng. **90**, 250–264 (2016)
20. Shyu, W.S., Teng, T.J., Chou, C.S.: Anti-plane response caused by interactions between a dike and the surrounding soil. Soil Dyn. Earthq. Eng. **92**, 408–418 (2017)
21. Shyu, W.S., Teng, T.J., Chou, C.S.: Effect of geometry on in-plane responses of a symmetric canyon subjected by P waves. Soil Dyn. Earthq. Eng. **113**, 215–229 (2018)

22. Shyu, W.S., Teng, T.J., Chai, J.F., Chou, C.S.: Determining anti-plane responses of a semi-circular alluvial valley embedded in a single layered half-space. Soil Dyn. Earthq. Eng. **131**, 106040 (2020)
23. Shyu, W.S., Teng, T.J., Chai, J.F., Chou, C.S.: Anti-plane responses induced by circular cavity beneath semi-circular canyon. J. Earthq. Eng. **26**(5), 2353–80 (2020)
24. Shyu, W.S., Chou, C.S., Lu, C.W.: Anti-plane responses of acceleration by a shallow hill next to an alluvial valley. Eng. Geol. **277**, 105777 (2020)
25. Montgometry, C.W.: Environmental Geology, McGrow Hill. (2014)
26. Thomson, W.T.: Transmission of elastic waves through a stratified solid. J. Appl. Phys. **21**, 89–93 (1950)
27. Kennett, B.L.N., Kerry, N.J.: Seismic waves in a stratified half space. Geophys. J. Int. **57**, 557–583 (1979)
28. Nguyen, C.T., Tassoulas, J.L.: Reciprocal absorbing boundary condition with perfectly matched discrete layers for the time-domain propagation of SH waves in a layered half-space. Soil Dyn. Earthq. Eng. **99**, 44–55 (2017)
29. Liang, J., Ba, Z.: Surface motion of an alluvial valley in layered half-space for incident plane SH waves. J. Earthq. Eng. Eng. Vib. **27**, 1–9 (2007). ((**in Chinese**))
30. Liang, J., Ba, Z.: Surface motion of a hill in layered half-space subjected to incident plane SH waves. J. Earthq. Eng. Eng. Vib. **28**, 1–10 (2008). ((**in Chinese**))
31. Liang, J., Ba, Z., Liu, Z.: Surface motion of an earth dam on layered half-space for incident plane SH waves, The 14th World Conference on Earthquake Engineering, Oct. 12–17, Beijing, China. (2008)
32. Liang, J., You, H., Lee, V.W.: Scattering of SV waves by a canyon in a fluid-saturated, poroelastic layered half-space, modeled using the indirect boundary element method. Soil Dyn. Earthq. Eng. **26**, 611–625 (2006)
33. Restrepo, D., Gómez, J.D., Jaramillo, J.D.: SH wave number Green's function for a layered, elastic half-space, part I: theory and dynamic canyon response by the discrete wave number boundary element method. Pure Appl. Geophys. **171**, 2185–2198 (2014)
34. Ba, Z., Sang, Q., Lee, V.W.: 2.5D scattering of obliquely incident seismic waves due to a canyon cut in a multi-layered TI saturated half-space. Soil Dyn. Earthq. Eng. **129**, 105957 (2020)
35. Ba, Z., Yin, X.: Wave scattering of complex local site in a layered half-space by using a multidomain IBEM: incident plane SH waves. Geophys. J. Int. **205**, 1382–1405 (2016)
36. Ba, Z., Liang, J., Zhang, Y.: Diffraction of SH-waves by topographic features in a layered transversely isotropic half-space. Earthq. Eng. Eng. Vib. **16**, 11–22 (2017)
37. Liu, G., Jiang, D.: Layer-effect on variable seismic ground motions of SV-wave scattered by a double-stratified circular-arc crossing by layer-interface. Soil Dyn. Earthq. Eng. **129**, 105919 (2020)
38. Liu, G., Feng, G.: Variable seismic motions of P-wave scattering by a layered V-shaped canyon of the second stratification type. Soil Dyn. Earthq. Eng. **144**, 106642 (2021)
39. Knupp, P., Steinberg, S.: Fundamentals of Grid Generation, CRC Press, Inc. (1994)